Electronic Supplementary Material (ESI) for Catalysis Science & Technology.

Electronic Supplementary Information (ESI)

Understanding Structure-Activity Relationships: Iron(II) Complexes of "Legacy Guanidines" as Catalysts for the Synthesis of Polylactide

Christian Conrads,[a] Lisa Burkart,[a] Sven Soerensen,[a] Sandra Noichl,[a] Yasemin Kara,[a] Joshua Heck,[a] Alexander Hoffmann[a] and Sonja Herres-Pawlis[a*]

[a]Institute of Inorganic Chemistry, RWTH Aachen University, Landoltweg 1a, 52074 Aachen, Germany

*** Correspondence:** Prof. Dr. Sonja Herres-Pawlis: sonja.herres-pawlis@ac.rwth-aachen.de

Table of Contents

1 Analytical Methods

1.1 Nuclear Magnetic Resonance Spectroscopy (NMR)

^{1}H NMR spectra were recorded on a Bruker Avance II 400, a Bruker Avance III HD400 or a Bruker Avance Neo 400 at 25 °C. For data acquisition, the software TopSpin was used (Bruker Avance II: TopSpin 2.1; Bruker Avance III: TopSpin 3.5 pl 7; Bruker Avance Neo: TopSpin 4.2.0). The analysis of data was performed with the software MestReNova.[1] The spectra were referenced to the residual solvent signal ($\delta(CHCl_3)$ = 7.26 ppm) relative to TMS.[2]

1.2 Single-Crystal X-Ray Diffraction (SC-XRD)

The acquired SC-XRD data are summarized in Tables S2 (**C1**–**C3**), S3 (**C4**–**C6**) and S4 (**C7**–**C8**). The data were collected with the four-circle goniometer Stoe Stadivari with Dectris Pilatus3 R 200 K hybrid pixel detector using Geni 3D high flux Mo-Kα radiation λ = 0.71073 Å, **C1** – **C5**, **C7**, **C8**) or Cu radiation (λ = 1.54186 Å, **C6**) at 100 K. The temperature control was achieved with an Oxford Cryostream 800. Crystals were mounted with grease on glass fibers. Data was collected with X-Area Pilatus[3, 4] and integrated with X-Area Integrate[5, 6] and X-Area Recipe[7, 8] .The spherical absorption correction was performed by Gaussian integration with Stoe X-Red32 followed by scaling of reflections with X-Area LANA[9, 10].

The structure was solved by direct and conventional Fourier methods and all non-hydrogen atoms were refined anisotropically with full-matrix least-squares based on F^2 (XPREP[11], SHELXS[12], SHELXT[13], ShelXle[14] and SHELXL[15]). Hydrogen atoms were derived from difference Fourier maps and placed at idealized positions, riding on their parent C atoms, with isotropic displacement parameters $U_{iso}(H) = 1.2\ U_{eq}(C)$ and $1.5\ U_{eq}(C_{methyl})$. All methyl groups were allowed to rotate but not to tip.

Full crystallographic data have been deposited with the Cambridge Crystallographic Data Centre as supplementary no. CCDC – 2278549 for **C1**, CCDC – 2278540 for **C2**, CCDC – 2278551 for **C3**, CCDC – 2278552 for **C4**, CCDC – 2278553 for **C5**, CCDC – 2278554 for **C6**, CCDC – 2278555 for **C7** and CCDC – 2278556 for **C8**. Copies of the data can be obtained free of charge by application to CCDC, 12 Union Road, Cambridge CB2 1EZ, UK (www.ccdc.cam.ac.uk/data_request/cif, e-mail: data_request@ccdc.cam.ac.uk).

1.3 Fourier-Transform Infrared Spectroscopy (FTIR)

FTIR spectra were recorded with a Shimadzu IRTracer-100 using a CsI beam splitter with an ATR unit (Quest model from Specac utilizing a robust monolithic crystalline diamond) with a resolution of 2 cm^{-1}. For data collection and the baseline correction, the software LabSolutions IR[16] was used. The peak picking and the assignment of intensities was carried out with the Spectra Editor integrated in the electronic lab notebook Chemotion.[17]

1.4 Matrix-Assisted Laser Desorption Ionization Time-of-Flight Mass Spectrometry (MALDI-TOF-MS)

The end group analysis was performed by MALDI-TOF-MS on a Bruker ultrafleXtreme equipped with a 337 nm smart beam laser in the reflective mode. THF solutions of *trans*-2-[3-(4-*tert*-butylphenyl)-2-methyl-2-propenylidene]malononitrile (DCTB) (5 µL of a 20 mg mL^{-1} solution), sodium trifluoroacetate (0.1 µL of a 10 mg mL^{-1} solution), and analyte (5 µL of a 10 mg mL^{-1} solution) were mixed and a droplet thereof applied on the sample target. The protein mixture *Protein 1 calibration standard* was used for calibration. For the spectra, 4000 laser shots with 24% laser power were collected. The laser repetition rate was 1000 Hz.

1.5 *In Situ* Raman Spectroscopy

Raman spectra were recorded under process conditions (135–180 °C, Ar atmosphere) using a RXN1 spectrometer of Kaiser Optical Systems with a 785 nm laser. The used detector is a TE-Cooled, 1024 CCD detector and the used stirrer corresponds to the model PRE1946 of Premex Reactor AG with a torsional moment

of 20 Ncm. An immersion probe with a sapphire lens (d = 0.1 mm) was applied to the autoclave optimized for monitoring biphasic reaction mixtures.[18] The data acquisition was done with the software iC Raman.[19] The obtained time-resolved data were processed with the PEAXACT software.[20] Characteristic peaks (lactide peak: 624–713 cm^{-1}, polylactide peak: 837–911 cm^{-1}) were integrated to receive the kinetic data.

1.6 Thermogravimetric Analysis (TGA)

Thermogravimetric analysis was conducted on a LINSEIS STA PT 1600 under a constant flow of nitrogen (60 sccm min^{-1}). The sample was heated from 29 K to 150 K with a heating rate of 5 K min^{-1} and was then kept at 150 °C for 1 h.

1.7 Differential Scanning Calorimetry (DSC)

DSC curves of selected polymer samples were recorded on a Netzsch DSC 204 F1 Phoenix equipped with an intra-cooler. The samples were weighed into 50 µL aluminum pans and sealed with punctuated aluminum lids. For all measurements, four cycles were performed, starting at 20 °C and subsequent heating to 200 °C. After each cooling, an isotherm at 20 °C was applied for 15 min. After the first heating, an isotherm at 200 °C was applied for 3 h. A heating rate of of 10 K min^{-1} and a nitrogen flow of 40 mL min^{-1} were applied. The analysis of data was performed with the software NETZSCH Proteus – Thermal Analysis.[21]

1.8 Elemental Analysis (EA)

Elemental analysis was performed on an elementar vario EL and an elementar vario EL cube.

1.9 Gel Permeation Chromatography (GPC)

The average molar masses and mass distributions of the polymer samples were determined by GPC. using a flow rate of 1 mL min^{-1} at 25 °C with THF as mobile phase. The utilized GPCmax VE-2001 from Viscotek is a combination of an HPLC pump, two Malvern Viscotek T columns (porous styrene divinylbenzene copolymer) with a maximum pore size of 500 and 5000 Å and a refractive index detector (VE-3580). A conventional calibration was applied to evaluate the chromatographic results. The analysis of data was performed with the software OmniSEC.[22] A correction factor of 0.58 was used according to literature for the molar mass of PLA relative to polystyrene standards.[23, 24]

1.10 Electrospray Ionization Mass Spectrometry (ESI-MS)

ESI-MS of the iron complexes was performed on an UHR-TOF Bruker Daltonik maXis II, an ESI-quadrupole time-of-flight (qToF) mass spectrometer capable of a resolution of at least 80.000 FWHM and a source voltage of 4.5 kV. Detection was in positive ion mode. The mass spectrometer was calibrated subsequently to every experiment via direct infusion of a L-proline sodium salt solution, which provided a m/z range of singly charged peaks up to 3000 Da in both ion modes.

1.11 Atmospheric Pressure Chemical Ionization Mass Spectrometry (APCI-MS)

APCI-MS of the iron complexes was performed on an UHR-TOF Bruker Daltonik maXis II using a source voltage of 4.0 kV with an end plate offset of -500 V. The corona current was set to 4000 nA. A nebulizer pressure of 3.0 bar was applied and a heater temperature of 300 °C. Detection was in positive ion mode.

2 Ligands

The guanidine ligands **L1**–**L8** were synthesized according to literature procedures starting from a commercially-available amine and *N*,*N*,*N*',*N*'-tetramethylchloroformamidinium chloride (TMG Vilsmeier salt) and *N*,*N*'-dimethylethylenechloroformamidinium chloride (DMEG Vilsmeier salt), respectively, which were prepared in the working group from phosgene and the respective urea according to literature.[25, 26] The chemical structures of the ligands **L1**–**L8** are depicted in Fig. S1 and the respective references are listed in Table S1 including the systematic IUPAC name and other trivial names that were used in literature for these compounds.

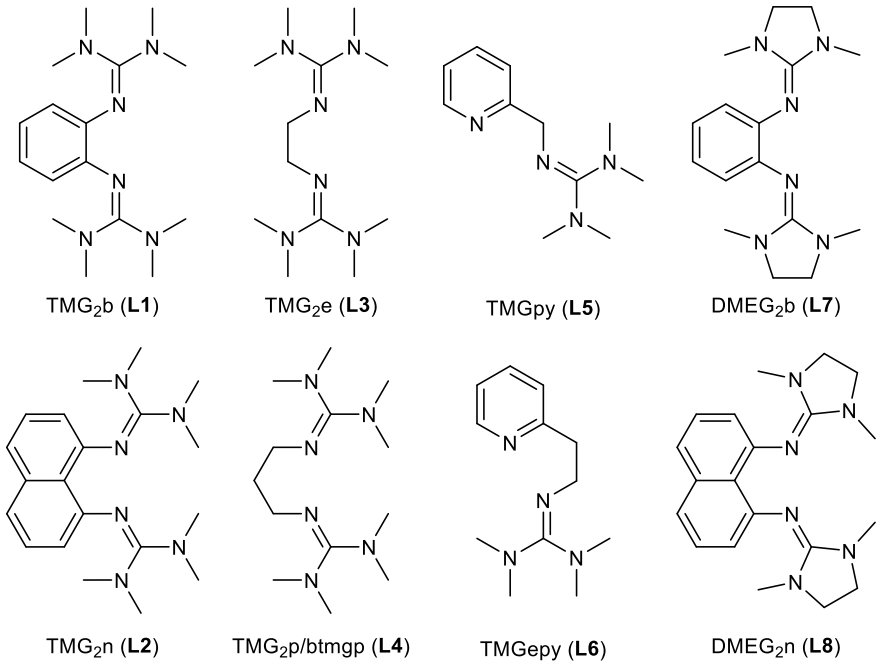

Fig. S1: Chemical structures of the guanidine ligands resynthesized in this work.

Table S1: References for the ligand synthesis.

Ligand	Other names	IUPAC name	Reference
TMG_2b (**L1**)	btmgb	2,2'-(1,2-Phenylene)bis(1,1,3,3-tetramethylguanidine)	[27]
TMG_2n (**L2**)	btmgn, TMGN	2',2'-(Naphthalene-1,8-diyl)bis(1,1,3,3-tetramethylguanidine)	[28]
TMG_2e (L3)		2',2'-(Ethane-1,2-diyl)bis(1,1,3,3-tetramethylguanidine)	[29]
TMG_2p (**L4**)	btmgp	2',2'-(Propane-1,3-diyl)bis(1,1,3,3-tetramethylguanidine)	[29, 30]
TMGpy (**L5**)		1,1,3,3-Tetramethyl-2-(pyridin-2-ylmethyl)guanidine	[31]
TMGepy (**L6**)		1,1,3,3-Tetramethyl-2-(2-(pyridin-2-yl)ethyl)guanidine	[32]
$DMEG_2b$ (**L7**)	bdmegb	N,N'-(1,2-phenylene)bis(1,3-dimethylimidazolidin-2-imine)	[33]
$DMEG_2n$ (**L8**)	DMEGN	N,N'-(naphthalene-1,8-diyl)bis(1,3-dimethylimidazolidin-2-imine)	[34]

3 Iron Complexes

3.1 Complex Synthesis

The experimental procedures for the synthesis of the iron complexes are described in the main paper and are additionally deposited in the Chemotion Repository. The links are given in the main paper.

3.2 Crystallographic Data

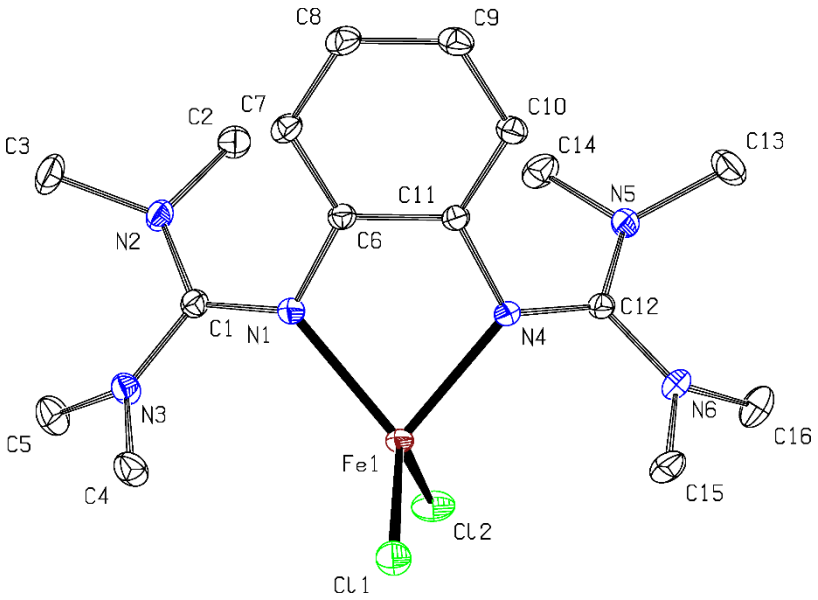

Fig. S2: Molecular structure of [Fe(TMG$_2$b)Cl$_2$] (**C1**) in the solid state (ellipsoids drawn with 50% probability level). Hydrogen atoms were omitted for clarity.

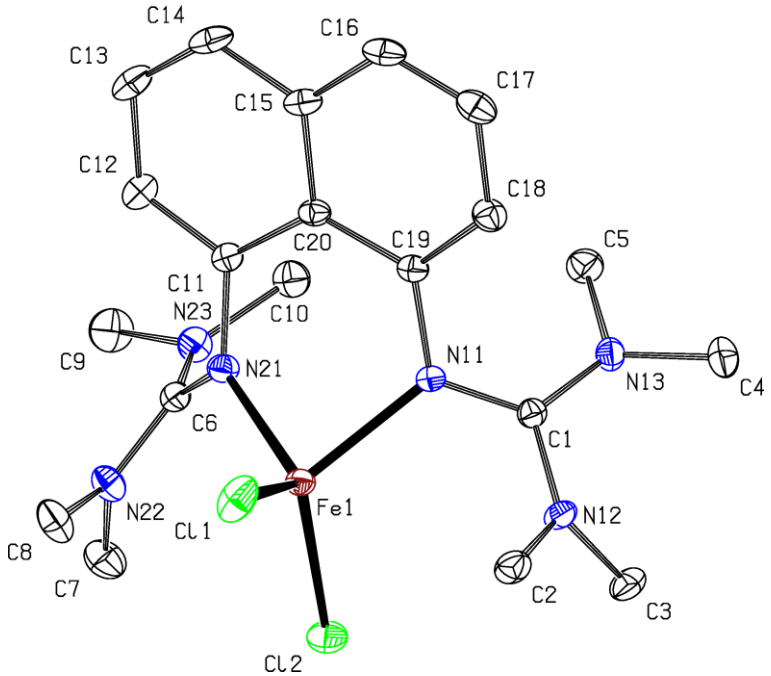

Fig. S3: Molecular structure of [Fe(TMG$_2$n)Cl$_2$] (**C2**) in the solid state (ellipsoids drawn with 50% probability level). Hydrogen atoms were omitted for clarity.

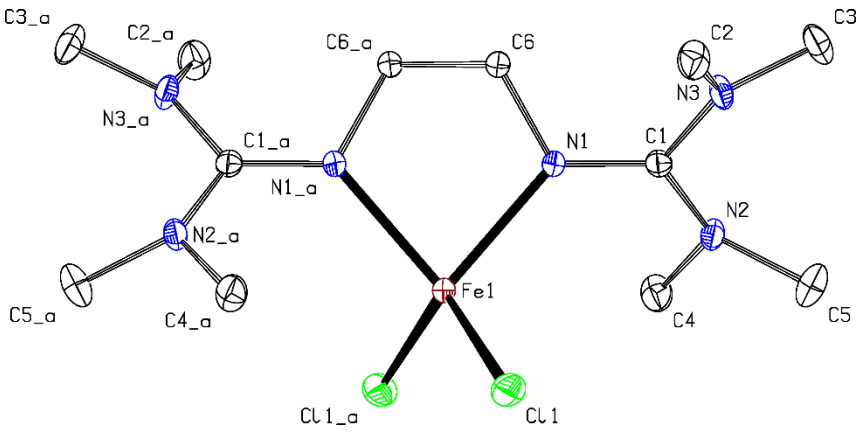

Fig. S4: Molecular structure of [Fe(TMG$_2$e)Cl$_2$] (**C3**) in the solid state (ellipsoids drawn with 50% probability level). Hydrogen atoms were omitted for clarity.

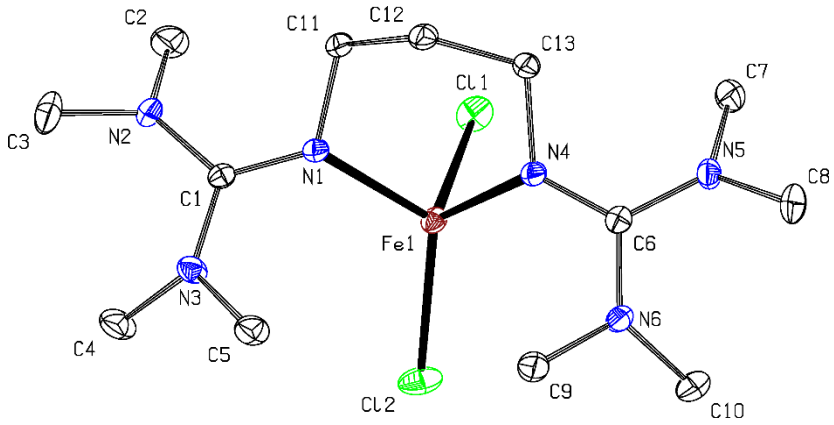

Fig. S5: Molecular structure of [Fe(TMG$_2$p)Cl$_2$] (**C4**) in the solid state (ellipsoids drawn with 50% probability level). Hydrogen atoms were omitted for clarity.

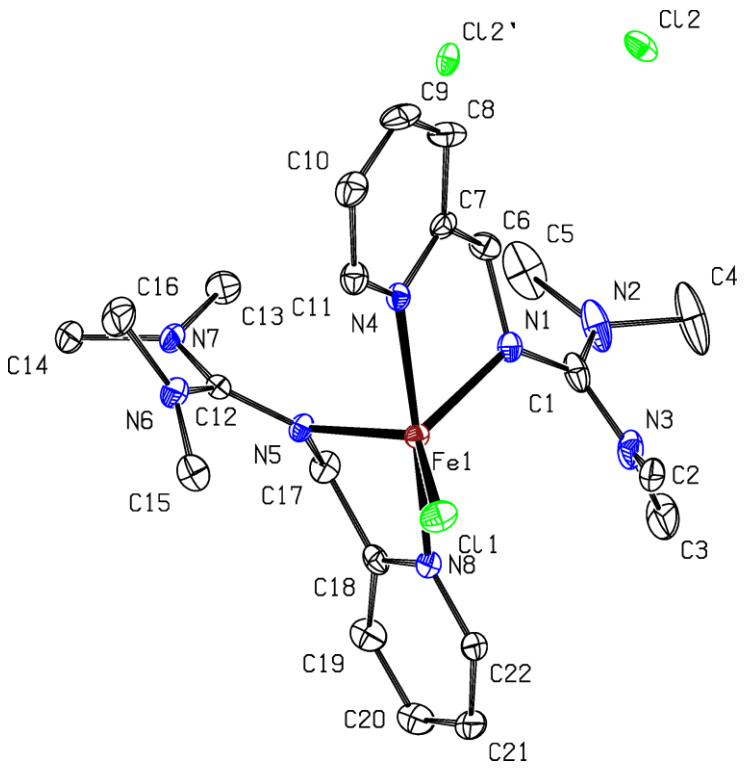

Fig. S6: Molecular structure of [Fe(TMGpy)$_2$Cl]Cl (**C5**) in the solid state (ellipsoids drawn with 50% probability level). Hydrogen atoms were omitted for clarity. The non-coordinating anion Cl2 is disordered.

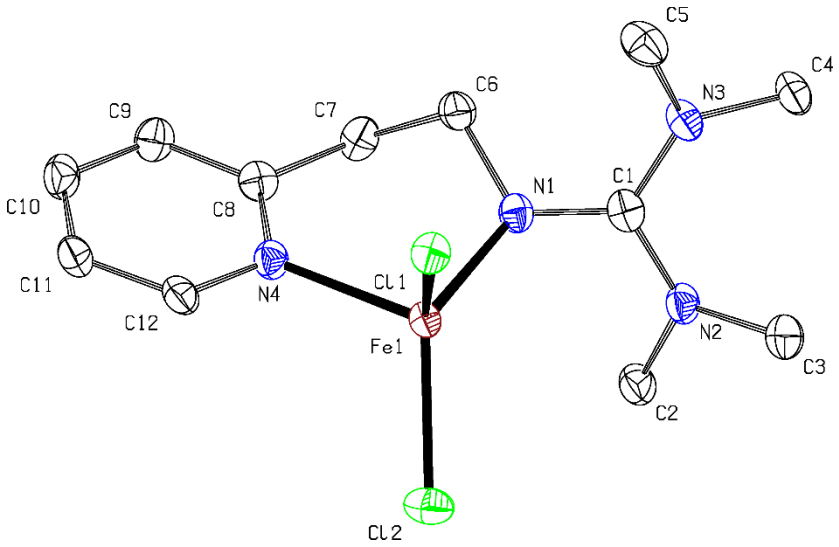

Fig. S7: Molecular structure of [Fe(TMGepy)Cl$_2$] (**C6**) in the solid state (ellipsoids drawn with 50% probability level). Hydrogen atoms were omitted for clarity.

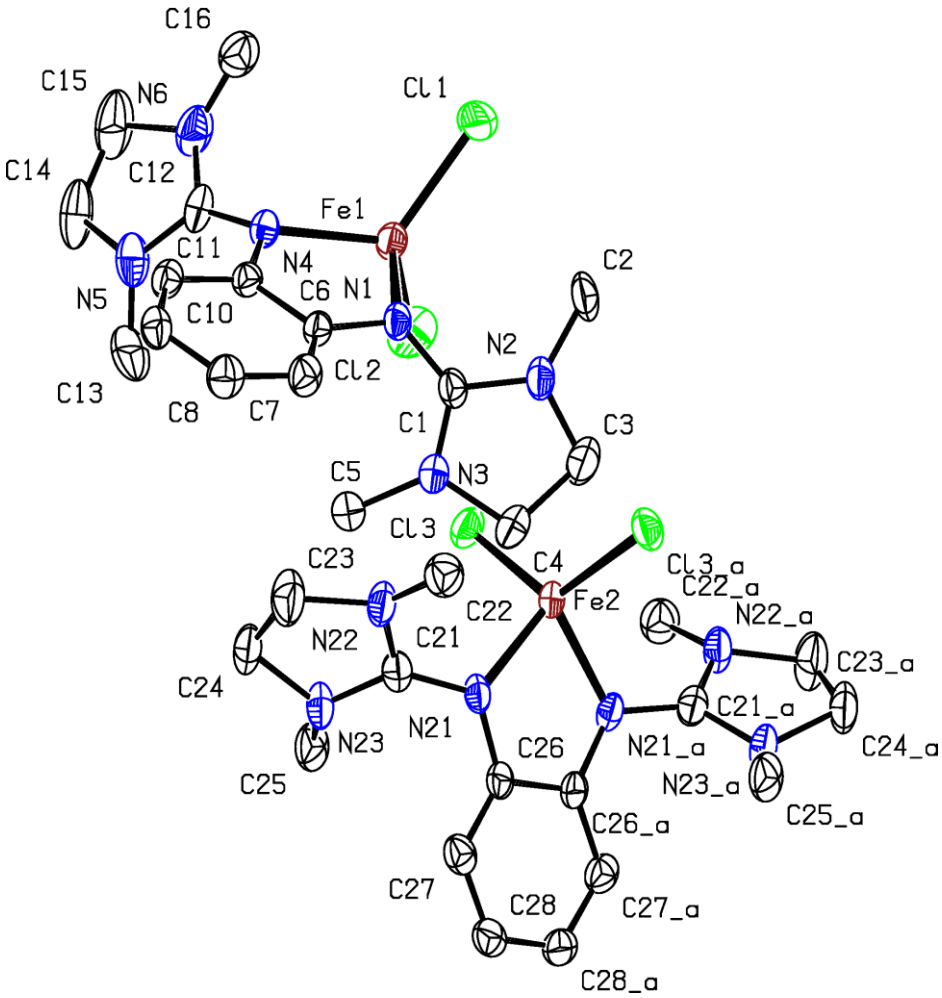

Fig. S8: Molecular structure of [Fe(DMEG$_2$b)Cl$_2$] (**C7**) in the solid state (ellipsoids drawn with 50% probability level). Hydrogen atoms were omitted for clarity.

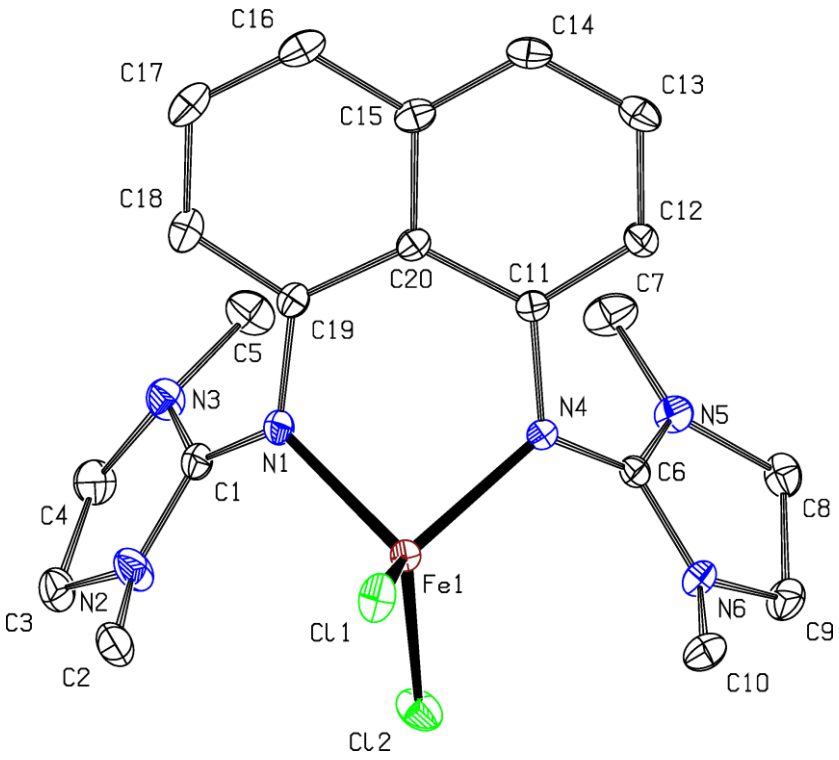

Fig. S9: Molecular structure of [Fe(DMEG$_2$n)Cl$_2$] (**C8**) in the solid state (ellipsoids drawn with 50% probability level). Hydrogen atoms were omitted for clarity.

Table S2: Crystallographic data of complexes **C1**–**C3**.

	C1	**C2**	**C3**
	[Fe(TMG$_2$b)Cl$_2$]	[Fe(TMG$_2$n)Cl$_2$]	[Fe(TMG$_2$e)Cl$_2$]
Empirical formula	$C_{16}H_{28}Cl_2FeN_6$	$C_{20}H_{30}Cl_2FeN_6$	$C_{12}H_{28}Cl_2FeN_6$
Formula weight [g mol^{-1}]	431.19	481.25	383.15
T [K]	100	100	100
λ [Å]	0.71073	0.71073	0.71073
Crystal system	monoclinic	monoclinic	monoclinic
Space group	$P2_1/c$	$P2_1/c$	$C2/c$
a [Å]	12.011(2)	11.288(2)	18.177(4)
b [Å]	10.508(2)	11.398(2)	7.3979(15)
c [Å]	16.725(3)	18.010(4)	13.815(3)
α [°]	90	90	90
β [°]	106.09(3)	94.59(3)	102.03(3)
γ [°]	90	90	90
V [Å^3]	2028.1(8)	2309.8(8)	1817.0(7)
Z	4	4	4
$\rho_{calc.}$ [g cm^{-1}]	1.412	1.384	1.401
μ [mm^{-1}]	1.019	0.903	1.127
F(000)	904	1008	808
Crystal size [mm]	0.260×0.200×0.160	0.190×0.180×0.170	0.140×0.130×0.120
hkl range	-14≤h≤18	-16≤h≤16	-18≤h≤28
	-15≤k≤15	-17≤k≤16	-11≤k≤11
	-25≤l≤25	-27≤1≤20	-21≤l≤21
Reflections collected	38281	28150	21888
Independent reflections	7950	8473	3454
R_{int}	0.0205	0.0432	0.0355
Number of parameters	234	270	100
R_1 [I>2σ(I)]	0.0303	0.0440	0.0239
wR_2 (all data)	0.0704	0.0985	0.0549
Goodness-of-fit	1.111	1.109	0.938
Largest diff. peak, hole [e Å^{-3}]	0.583	0.482	0.445
	-0.396	-0.420	-0.325

Table S3: Crystallographic data of complexes **C4**–**C6**.

	C4	**C5**	**C6**
	[Fe(TMG$_2$p)Cl$_2$]	**[Fe(TMGpy)$_2$Cl]Cl**	**[Fe(TMGepy)Cl$_2$]**
Empirical formula	$C_{13}H_{30}Cl_2FeN_6$	$C_{22}H_{36}Cl_2FeN_8$	$C_{12}H_{20}Cl_2FeN_4$
Formula weight [g mol^{-1}]	397.18	539.34	347.07
T [K]	100	100	100
λ [Å]	0.71073	0.71073	1.54186
Crystal system	triclinic	orthorhombic	orthorhombic
Space group	$P\bar{1}$	$P2_12_12_1$	$P2_12_12_1$
a [Å]	9.3007(19)	12.769(3)	8.7832(18)
b [Å]	9.830(2)	13.649(3)	11.895(2)
c [Å]	12.490(3)	15.343(3)	15.221(3)
α [°]	69.47(3)	90	90
β [°]	87.94(3)	90	90
γ [°]	65.38(3)	90	90
V [Å^3]	964.0(4)	2674.1(9)	1590.3(6)
Z	2	4	4
$\rho_{calc.}$ [g cm^{-1}]	1.368	1.340	1.450
μ [mm^{-1}]	1.065	0.790	10.630
F(000)	420	1136	720
Crystal size [mm]	0.180×0.150×0.110	0.210×0.180×0.160	0.320×0.220×0.130
hkl range	-14≤h≤12	-19≤h≤18	-10≤h≤7
	-14≤k≤15	-21≤k≤20	-14≤k≤13
	-19≤l≤19	-21≤l≤23	-17≤l≤18
Reflections collected	23563	35928	25688
Independent reflections	7566	9889	2964
$R_{int.}$	0.0254	0.1038	0.0453
Number of parameters	207	316	176
R_1 [I>2σ(I)]	0.0265	0.0454	0.0370
wR_2 (all data)	0.0657	0.0931	0.1020
Goodness-of-fit	0.963	0.933	1.074
Largest diff. peak, hole [e Å^{-3}]	0.406	0.784	0.390
	-0.329	-0.826	-0.737
Absolute structure parameter		-0.006(7)	0.001(5)

Table S4: Crystallographic data of complexes **C7**–**C8**.

	C7 **[Fe(DMEG$_2$b)Cl$_2$]**	**C8** **[Fe(DMEG$_2$n)Cl$_2$]**
Empirical formula	$C_{16}H_{24}Cl_2FeN_6$	$C_{20}H_{26}Cl_2FeN_6$
Formula weight [g mol^{-1}]	427.16	477.22
T [K]	100	100
λ [Å]	0.71073	0.71073
Crystal system	monoclinic	monoclinic
Space group	*I*2/*a*	$P2_1/c$
a [Å]	17.306(4)	15.712(3)
b [Å]	9.4540(19)	9.2900(19)
c [Å]	36.444(11)	16.520(3)
α [°]	90	90
β [°]	97.32(3)	116.37(3)
γ [°]	90	90
V [Å^3]	5914(3)	2160.4(9)
Z	12	4
$\rho_{calc.}$ [g cm^{-1}]	1.439	1.467
μ [mm^{-1}]	1.048	0.965
F(000)	2664	992
Crystal size [mm]	0.240×0.210×0.170	0.210×0.200×0.180
hkl range	-22≤h≤22	-12≤h≤25
	-11≤k≤12	-15≤k≤15
	35≤l≤46	-27≤l≤23
Reflections collected	28817	109748
Independent reflections	6436	9941
$R_{int.}$	0.1453	0.1128
Number of parameters	345	266
R_1 [$I>2\sigma(I)$]	0.0648	0.0359
wR_2 (all data)	0.1933	0.0940
Goodness-of-fit	1.025	1.057
Largest diff. peak, hole [e Å^{-3}]	1.619	0.622
	-0.768	-0.903

3.3 Thermogravimetric Analysis (TGA)

3.3.1 General Remarks on TGA Measurements

In order to investigate the thermal stability of the eight iron guanidine complexes **C1**–**C8,** TGA measurements were conducted (see Fig. S10 and S14– S20). For **C2**–**C8**, no significant mass loss was observed. For the complex formed from $FeCl_2$ and TMG_2b (**L1**), a mass loss of approximately 8% was observed beginning at a temperature of approximately 125 °C. This indicates the existence of a solvate of **C1**. Indeed, SC-XRD of a different single-crystal revealed the existence of an acetonitrile solvate $[Fe(TMG_2b)Cl_2]\cdot 1.5MeCN$ (**C1**·1.5MeCN) that may form under the same crystallization conditions. The overall quality of the dataset of **C1**·1.5MeCN is poor due to the crystal quality and only the connectivity could be obtained. The amount of the non-coordinating solvent is roughly determined to 1.5 equivalents per complex molecule. Also, the IR spectra before and after TGA show a slight difference (see Fig. S11–S12) and the IR spectrum after TGA resembles the spectrum recorded for the single-crystal of acetonitrile-free **C1** (see Fig. S13).

3.3.2 Plots of TGA Measurements

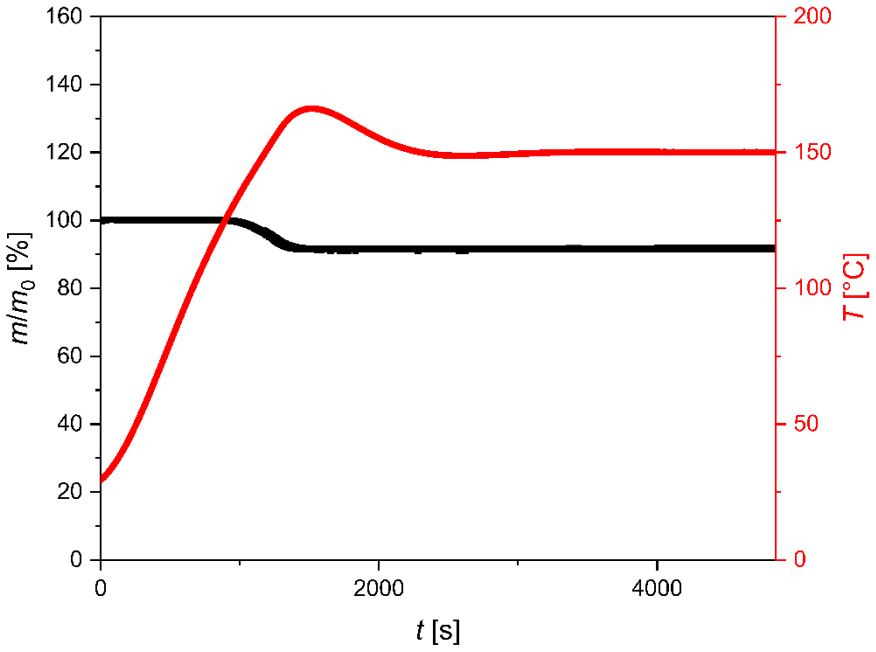

Fig. S10: TGA of $[Fe(TMG_2b)Cl_2]\cdot 1.5MeCN$ (**C1**·1.5MeCN). A mass loss of approximately 8% was observed beginning at a temperature of approximately 125 °C.

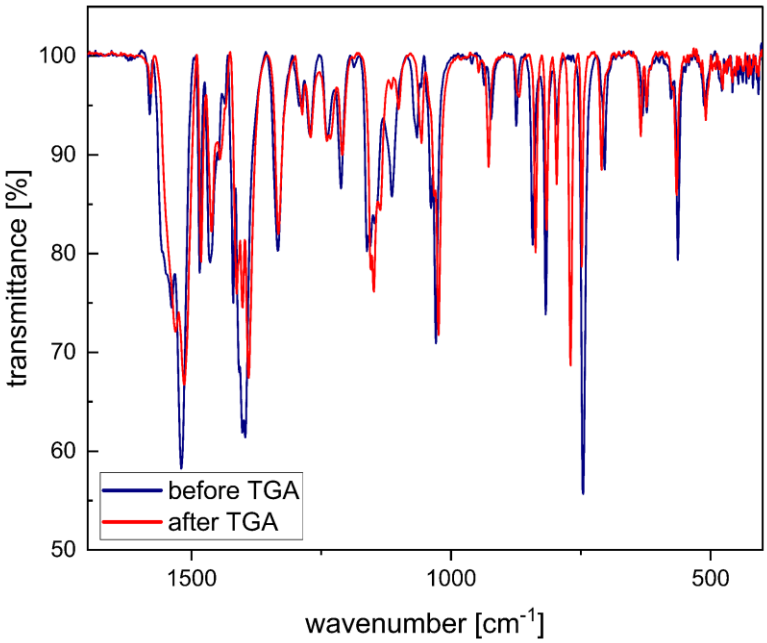

Fig. S11: IR spectra recorded for [Fe(TMG$_2$b)Cl$_2$]·1.5MeCN (**C1**·1.5MeCN) before and after TGA. For clarity, only the wavenumber range from 400 to 1700 cm^{-1} is depicted. The spectra deviate slightly indicating different species before and after TGA. Most strikingly, during TGA a new peak at 770 cm^{-1} appears (see expansion in Fig. S12). The spectrum after TGA matches the spectrum of the complex [Fe(TMG$_2$b)Cl$_2$] (**C1**) without acetonitrile (see Fig. S13).

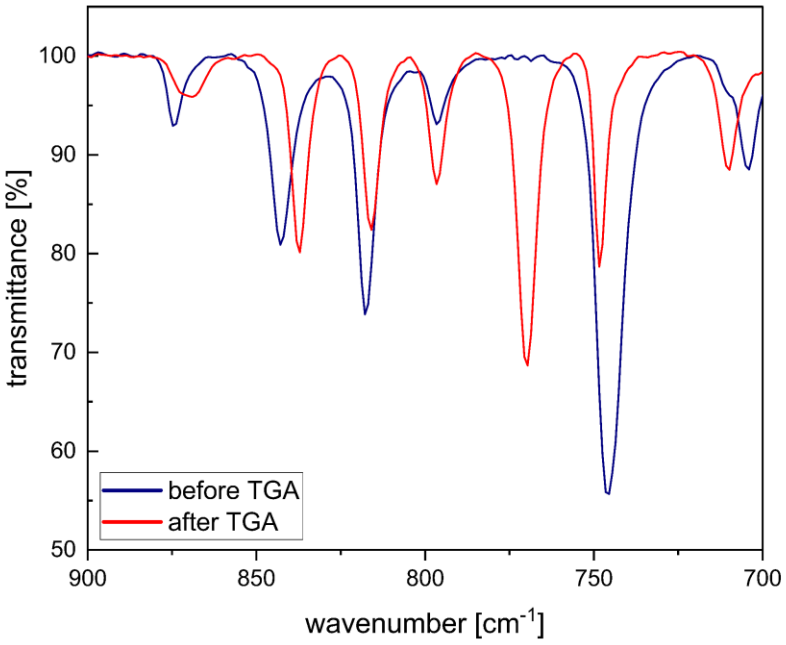

Fig. S12: IR spectra recorded for [Fe(TMG$_2$b)Cl$_2$]·1.5MeCN (**C1**·1.5MeCN) before and after TGA (expansion).

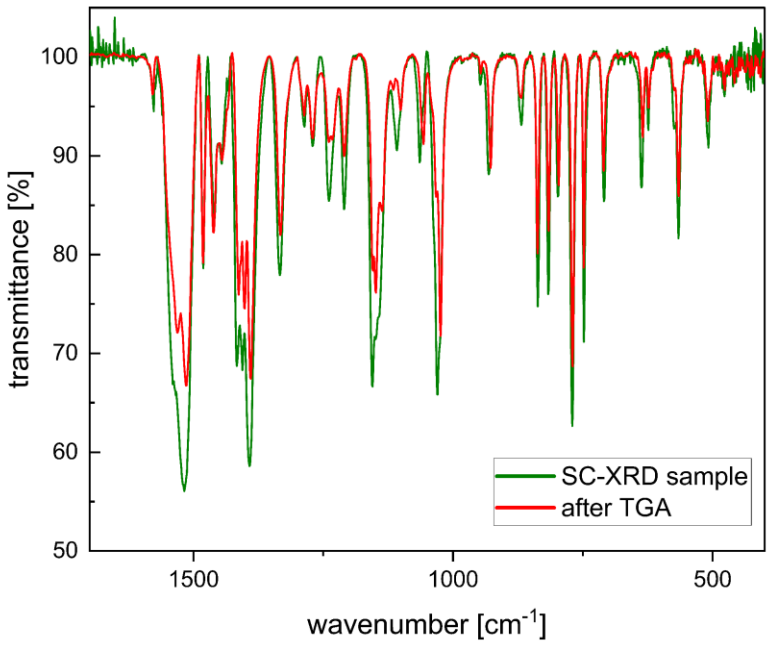

Fig. S13: IR spectra of [Fe(TMG$_2$b)Cl$_2$] (**C1**, structure of sample confirmed by SC-XRD) and of **C1**·1.5MeCN after TGA. For clarity only the wavenumber range from 400 to 1700 cm^{-1} is depicted. Both spectra match indicating that the solvate **C1**·1.5MeCN can be transferred into the acetonitrile-free **C1** by heating.

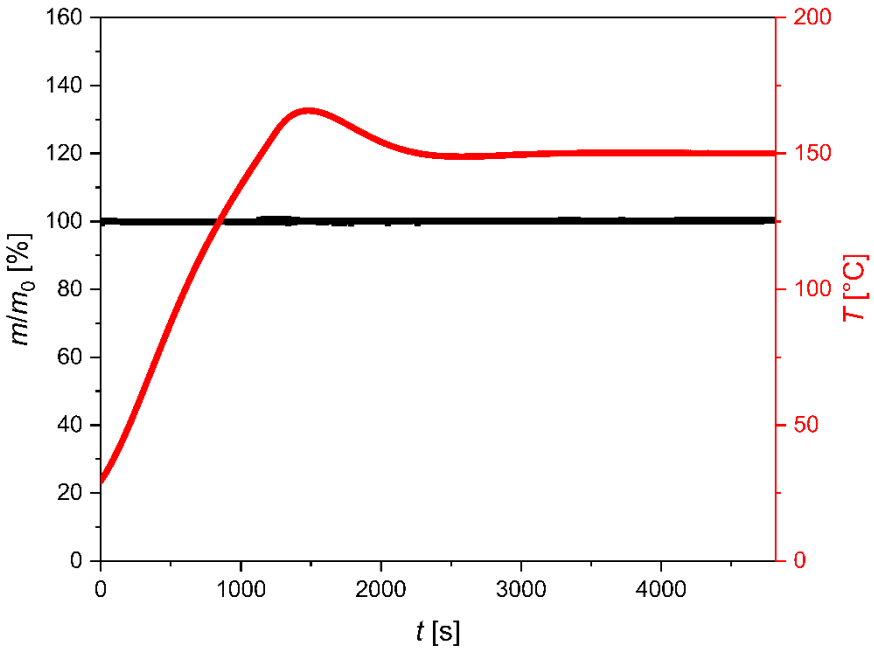

Fig. S14: TGA of [Fe(TMG$_2$n)Cl$_2$] (**C2**).

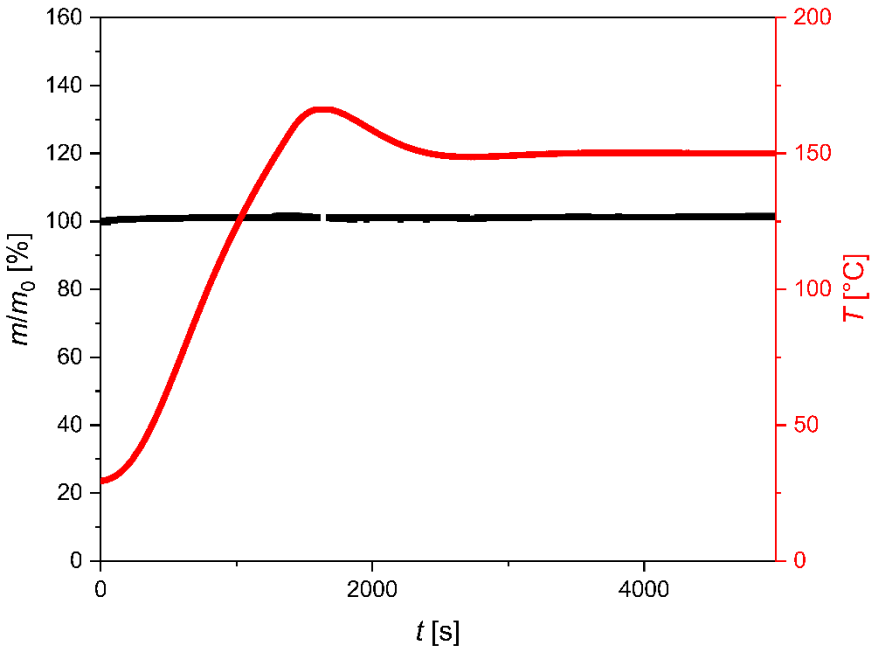

Fig. S15: TGA of [Fe(TMG$_2$e)Cl$_2$] (**C3**).

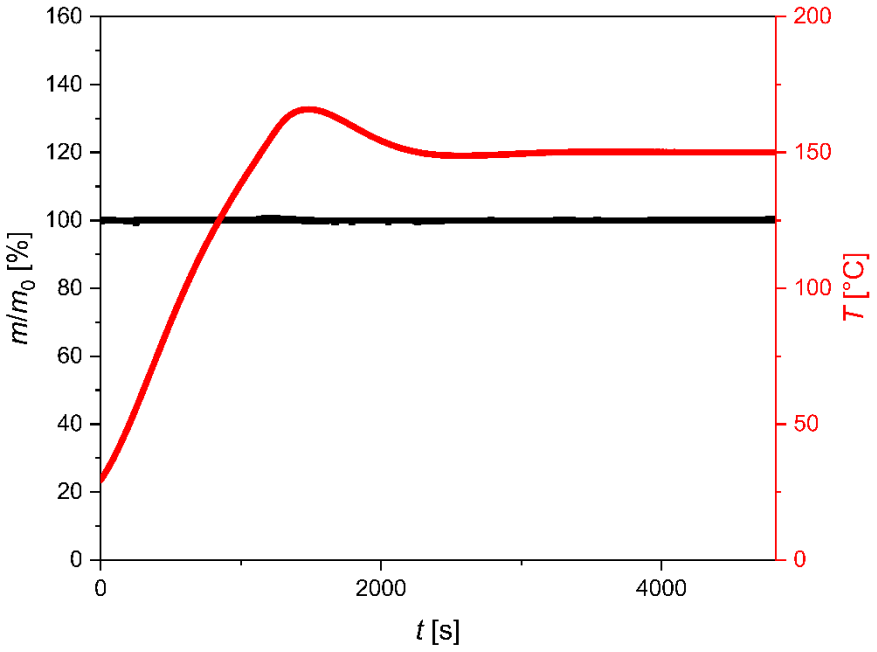

Fig. S16: TGA of [Fe(TMG$_2$p)Cl$_2$] (**C4**).

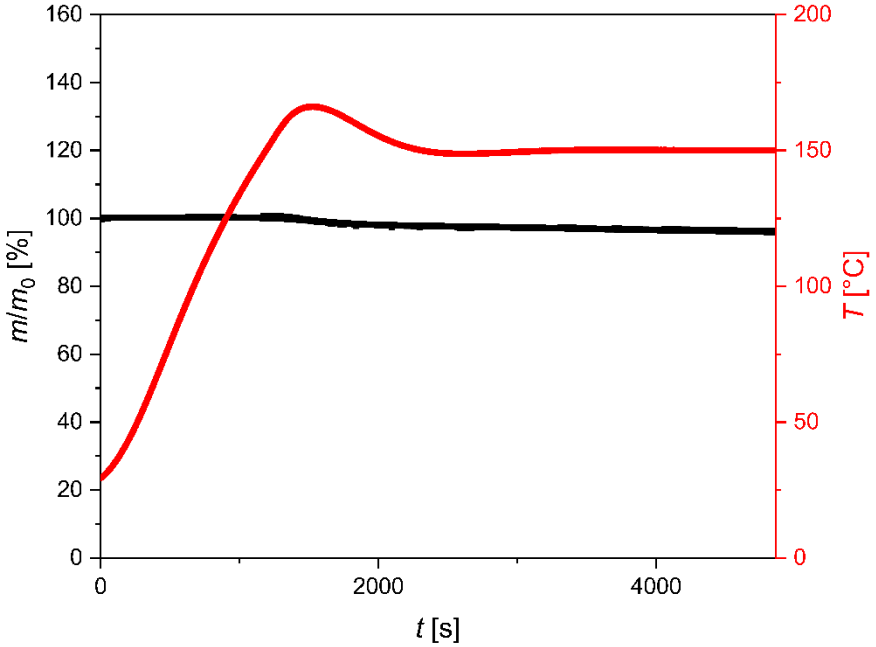

Fig. S17: TGA of $[Fe(TMGpy)_2Cl]Cl$ (**C5**).

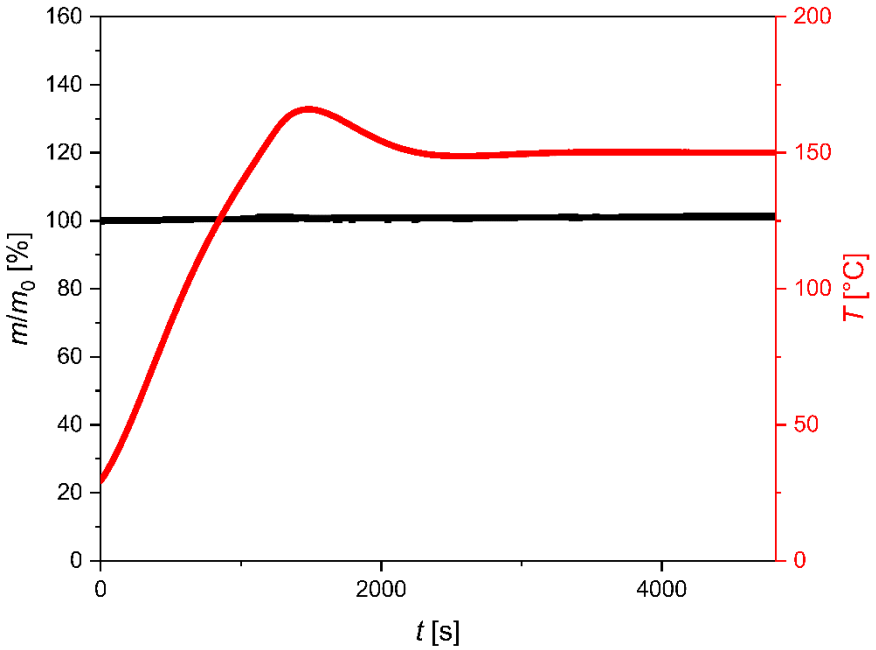

Fig. S18: TGA of $[Fe(TMGepy)Cl_2]$ (**C6**).

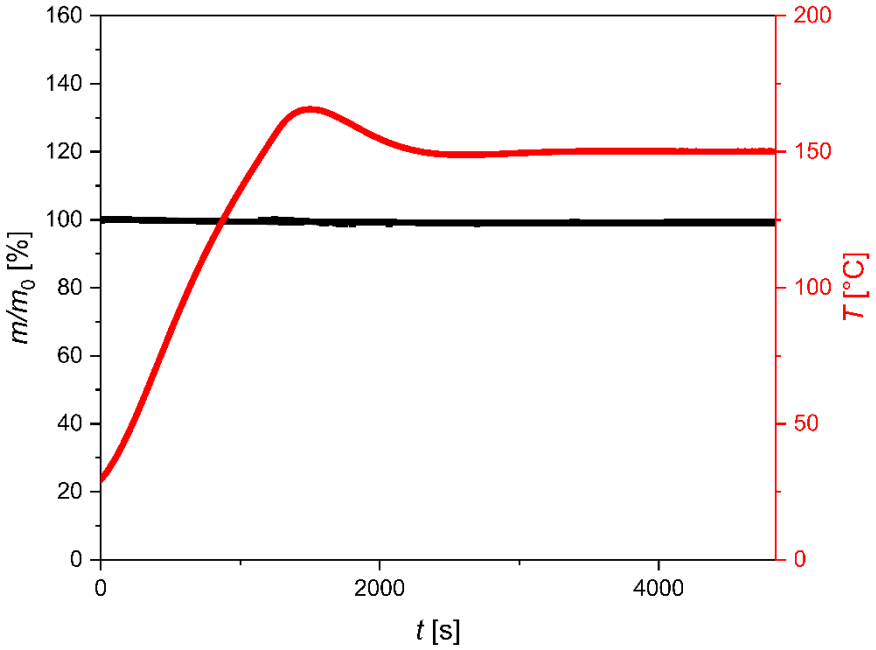

Fig. S19: TGA of [Fe(DMEG$_2$b)Cl$_2$] (**C7**).

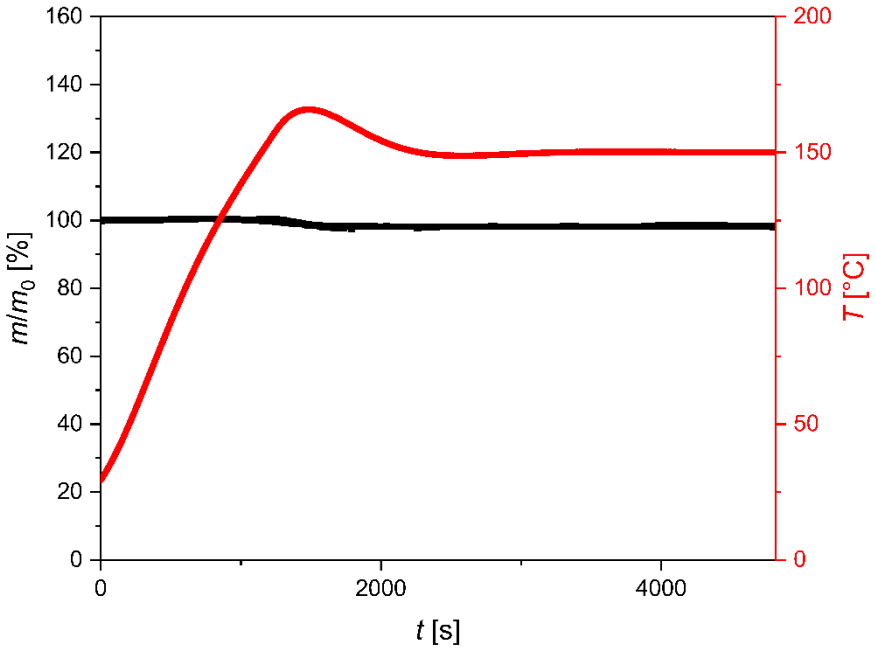

Fig. S20: TGA of [Fe(DMEG$_2$n)Cl$_2$] (**C8**)

4 Polymerization Experiments

The following Tables S5–S9 summarize all polymerization experiments that were conducted. The reaction times *t*, the conversion *p*, the initial apparent rate constants k_{app}, the theoretical molar masses $M_{n,theo}$, the experimental molar masses M_n and M_w and the dispersities M_w/M_n are given. The semilogarithmic plots from which the apparent rate constants k_{app} were determined are given below in Section 4.3.

4.1 Tables of Polymerization Experiments, Conversions, k_{app} Values and GPC Results

Table S5: Polymerization experiments for the evaluation of the catalyst activity.[a]

No.	Cat.	[M]/[I]	*t* [min]	*p*[b] [%]	k_{app}[c] [10^{-4} s^{-1}]	$M_{n,theo}$[d] [kg·mol^{-1}]	M_n[e] [kg·mol^{-1}]	M_w[e] [kg·mol^{-1}]	M_w/M_n[e]	Fig.
1	**C1**	1000/1	300	11	0.0583	15.9	n. d.[f]	n. d.[f]	n. d.[f]	S22
2	**C1**	1000/1	300	13	0.0675	18.7	n. d.[f]	n. d.[f]	n. d.[f]	S23
3	**C2**	1000/1	300	65	0.648	93.7	25.0	37.1	1.5	S24
4	**C2**	1000/1	300	49	0.502	70.6	11.2	16.4	1.5	S25
5	**C3**	1000/1	60	56	9.67	80.7	25.3	37.3	1.5	S26
6	**C3**	1000/1	60	55	9.59	79.3	20.2	32.8	1.6	S27
7	**C4**	1000/1	60	42	40.1	60.5	14.1	20.6	1.5	S28
8	**C4**	1000/1	60	55	68.3	79.3	21.2	30.8	1.5	S29
9	**C5**	1000/1	60	41	2.09	59.1	11.0	15.9	1.4	S30
10	**C5**	1000/1	60	38	2.61	54.8	8.2	11.9	1.4	S31
11	**C6**	1000/1	10	59	24.0	85.0	47.3	68.4	1.4	S32
12	**C6**	1000/1	10	61	24.3	87.9	42.2	59.8	1.4	S33
13	**C7**	1000/1	300	7	0.0279	10.1	n. d.[f]	n. d.[f]	n. d.[f]	S34
14	**C7**	1000/1	300	12	0.0280	17.3	n. d.[f]	n. d.[f]	n. d.[f]	S35
15	**C8**	1000/1	300	80	1.34	115.3	45.7	69.4	1.5	S36
16	**C8**	1000/1	300	77	1.31	111.0	34.7	53.4	1.5	S37
17	$FeCl_2$	1000/1	300	16	0.0871	23.1	n. d.[f]	n. d.[f]	n. d.[f]	S38
18	$FeCl_2$	1000/1	300	13	0.0701	18.7	n. d.[f]	n. d.[f]	n. d.[f]	S39
19	none	n/a	300	0	n/a	n/a	n. d.[f]	n. d.[f]	n. d.[f]	S40
20	none	n/a	300	0	n/a	n/a	n. d.[f]	n. d.[f]	n. d.[f]	S40

[a] Polymerization conditions: 8.00 g (55.5 mmol) recrystallized L-lactide, *T* = 150 °C, stirring speed: 260 rpm, argon atmosphere. [b] Conversions were determined from the ^{1}H NMR spectrum of the polymerization mixture. [c] Initial apparent polymerization rate constant determined from the linear region of the semilogarithmic plots of ln(1/(1-*p*)) vs. *t*. [d] Theoretical molar mass, $M_{n,theo}$ = [M]/[I]·*M*(LA)·*p*. [e] Determined by GPC with THF as eluent. A conventional calibration with polystyrene standards was used and the molar masses were corrected by a factor of 0.58.[23, 24] [f] The molar mass was not determined because no precipitation from EtOH at 20 °C was observed.

Table S6: Additional polymerization experiments with [Fe(TMG$_2$e)Cl$_2$] (**C3**).[a]

No.	Cat.	CoI/ Additive	[M]/[I] /[CoI]	*t* [min]	*p*[b] [%]	k_{app}[c] [10^{-4} s^{-1}]	$M_{n,theo}$[d] [kg·mol^{-1}]	M_n[e] [kg· mol^{-1}]	M_w[e] [kg· mol^{-1}]	M_w/ M_n[e]	Fig.
1	$FeCl_2$	TMG$_2$e	1000/1/1	60	25	1.22	36.0	3.0	3.5	1.2	S41
2	**C3**	*p*MeBnOH	1000/1/1	60	63	10.1	45.4	33.7	41.8	1.2	S42
3	**C3**	TMG$_2$e (**L3**)	1000/1/1	60	45	19.8	64.9	8.1	11.2	1.4	S43
4	**C3**	$FeCl_2$	1000/1/1	60	76	8.79	109.5	67.7	104.0	1.5	S44
5	–	TMG$_2$e	1000/1	60	11	0.0351	15.9	n. d.[f]	n. d.[f]	n. d.[f]	S45
6	**C3**	–	500/1	60	80	14.8	57.7	46.2	65.5	1.4	S46

[a] Polymerization conditions: 8.00 g (55.5 mmol) recrystallized L-lactide, T = 150 °C, stirring speed: 260 rpm, argon atmosphere. [b] Conversions were determined from the ^{1}H NMR spectrum of the polymerization mixture. [c] Initial apparent polymerization rate constant determined from the linear region of the semilogarithmic plots of ln(1/(1-p)) vs. t. [d] Theoretical molar mass, $M_{n,theo}$ = [M]/[I]·M(LA)·p. For polymerizations involving a co-initiator: $M_{n,theo}$ = [M]/([CoI]+[I])·M(LA)·p. $FeCl_2$ was not considered as a co-initiator. [e] Determined by GPC with THF as eluent. A conventional calibration with polystyrene standards was used and the molar masses were corrected by a factor of 0.58.[23, 24] [f] The molar mass was not determined because no precipitation from EtOH at 20 °C was observed.

Table S7: Experiments for the k_p determination with [Fe(TMGepy)Cl$_2$] (**C6**).[a]

No.	Cat.	[M]/[I]	*t* [min]	*p*[b] [%]	k_{app}[c] [10^{-4} s^{-1}]	$M_{n,theo}$[d] [kg·mol^{-1}]	M_n[e] [kg·mol^{-1}]	M_w[e] [kg·mol^{-1}]	M_w/ M_n[e]	Fig.
1	**C6**	1000/1	10	59	24.0	85.0	47.3	68.4	1.4	S32
2	**C6**	1000/1	10	61	24.3	87.9	42.2	59.8	1.4	S33
3	**C6**	1250/1	30	59	16.6	106.3	41.1	63.2	1.5	S47
4	**C6**	1500/1	30	46	12.5	99.4	33.5	46.8	1.4	S48
5	**C6**	2000/1	60	44	8.47	126.8	29.9	44.8	1.5	S49
6	**C6**	5000/1	60	12	0.589	86.5	n. d.[f]	n. d.[f]	n. d.[f]	S50
7	**C6**	5000/1	60	12	0.714	86.5	n. d.[f]	n. d.[f]	n. d.[f]	S51

[a] Polymerization conditions: 8.00 g (55.5 mmol) recrystallized L-lactide, T = 150 °C, stirring speed: 260 rpm, argon atmosphere. [b] Conversions were determined from the ^{1}H NMR spectrum of the polymerization mixture. [c] Initial apparent polymerization rate constant determined from the linear region of the semilogarithmic plots of ln(1/(1-p)) vs. t. [d] Theoretical molar mass, $M_{n,theo}$ = [M]/[I]·M(LA)·p. [e] Determined by GPC with THF as eluent. A conventional calibration with polystyrene standards was used and the molar masses were corrected by a factor of 0.58.[23, 24] [f] The molar mass was not determined because no precipitation from EtOH at 20 °C was observed.

Table S8: Additional experiments with **C4** and **C6** at different temperatures and varying lactide purities.[a]

No.	Cat.	[M]/[I]	t [min]	T [°C]	p[b] [%]	k_{app}[c] [10^{-4} s^{-1}]	$M_{n,theo}$[d] [kg·mol^{-1}]	M_n[e] [kg·mol^{-1}]	M_w[e] [kg·mol^{-1}]	M_w/ M_n[e]	Fig.
1[f]	**C4**	1000/1	60	150	49	42.3	70.6	17.8	24.9	1.4	S52
2[f]	**C6**	1000/1	10	150	67	24.8	96.6	55.1	82.1	1.5	S53
3	**C6**	1000/1	10	135	16	4.40	23.1	19.9	29.7	1.5	S54
4	**C6**	1000/1	10	180	71	39.8	102.3	42.8	63.0	1.5	S55
5	**C6**	2000/1	60	180	65	22.1	187.4	26.2	40.8	1.6	S56
6[f]	**C6**	2000/1	60	150	60	11.4	173.0	57.5	86.7	1.5	S57
7[g]	**C6**	2000/1	60	150	63	6.89	181.6	29.1	47.8	1.6	S58

[a] Polymerization conditions: 8.00 g (55.5 mmol) recrystallized L-lactide, T = 150 °C, stirring speed: 260 rpm, argon atmosphere. [b] Conversions were determined from the ^{1}H NMR spectrum of the polymerization mixture. [c] Initial apparent polymerization rate constant determined from the linear region of the semilogarithmic plots of ln(1/(1-p)) vs. t. [d] Theoretical molar mass, $M_{n,theo}$ = [M]/[I]·M(LA)·p. [e] Determined by GPC with THF as eluent. A conventional calibration with polystyrene standards was used and the molar masses were corrected by a factor of 0.58 [23, 24]. [f] L-lactide was recrystallized from toluene and subsequently sublimated. [g] Technical-grade *rac*-lactide was used without further purification.

Table S9: Polymerization experiments with [Fe(TMGepy)Cl_2] (**C6**) with co-initiator.[a]

No.	Cat.	CoI/ Additive	[M]/[I] /[CoI]	t [min]	p[b] [%]	k_{app}[c] [10^{-4} s^{-1}]	$M_{n,theo}$[d] [kg·mol^{-1}]	M_n[e] [kg·mol^{-1}]	M_w[e] [kg·mol^{-1}]	M_w/ M_n[e]	Fig.
1	**C6**	*p*MeBnOH	2000/1/1	60	68	17.8	98.0	68.3	92.5	1.4	S59
2	**C6**	*p*MeBnOH	2000/1/4	60	75	27.8	43.2	48.7	60.9	1.3	S60
3	**C6**	*p*MeBnOH	5000/1/5	60	34	6.02	40.8	26.9	32.4	1.2	S61
4	**C6**	$FeCl_2$	2000/1/1	60	65	11.0	187.4	68.5	97.9	1.4	S62

[a] Polymerization conditions: 8.00 g (55.5 mmol) recrystallized L-lactide, T = 150 °C, stirring speed: 260 rpm, argon atmosphere. [b] Conversions were determined from the ^{1}H NMR spectrum of the polymerization mixture. [c] Initial apparent polymerization rate constant determined from the linear region of the semilogarithmic plots of ln(1/(1-p)) vs. t. [d] Theoretical molar mass, $M_{n,theo}$ = [M]/[I]·M(LA)·p. For polymerizations involving a co-initiator: $M_{n,theo}$ = [M]/([CoI]+[I])·M(LA)·p. $FeCl_2$ was not considered as a co-initiator. [e] Determined by GPC with THF as eluent. A conventional calibration with polystyrene standards was used and the molar masses were corrected by a factor of 0.58.[23, 24]

4.2 Determination of Conversion by ^{1}H NMR Spectroscopy

The conversion of lactide was determined by ^{1}H NMR spectroscopy as depicted in Fig. S21. The integrals of the methine signals of the monomer (1') and the polymer (1) were used.

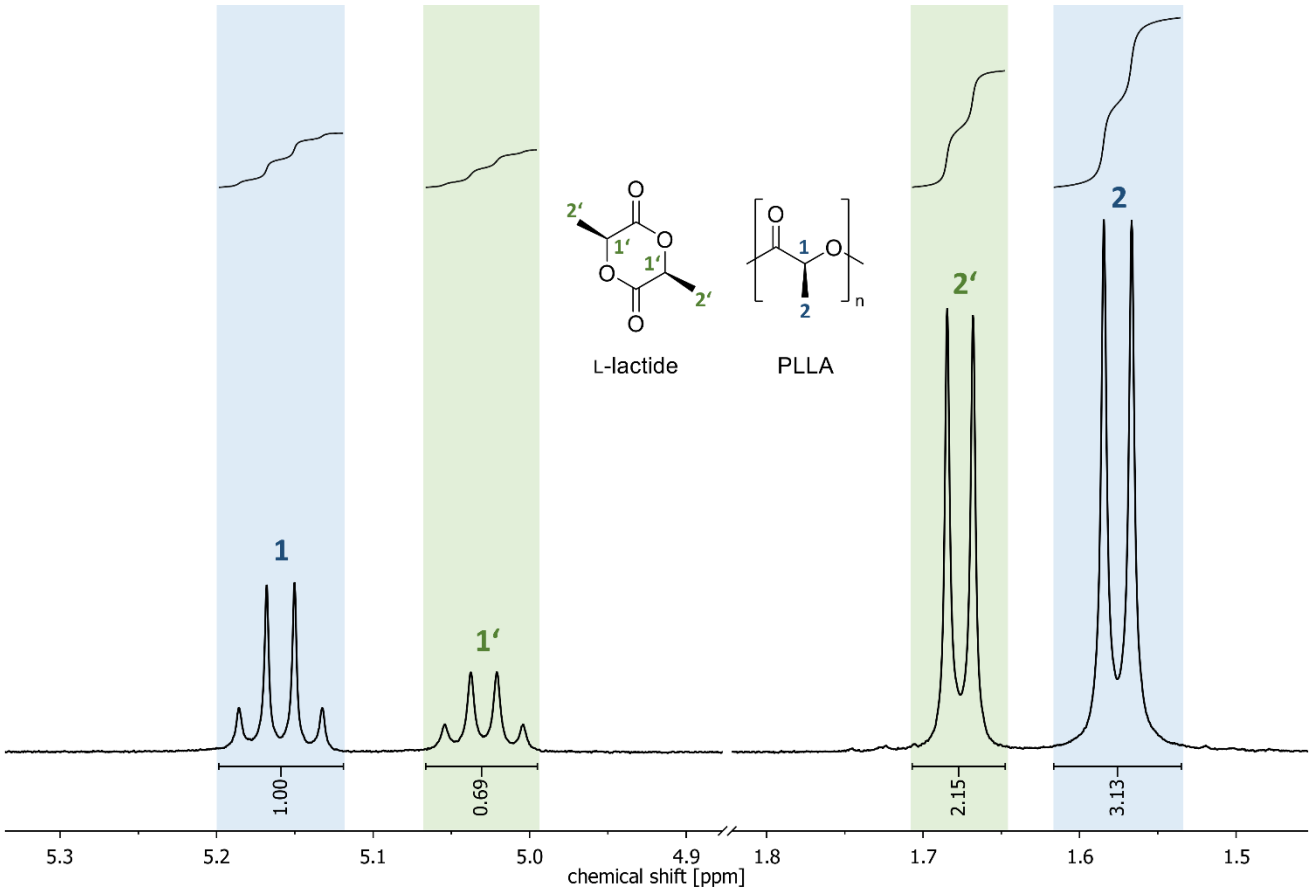

Fig. S21: ^{1}H NMR spectrum ($CDCl_3$) of the polymerization of L-lactide (LLA) with **C6** ([LLA]/[**C6**] = 1000:1, 10 min, 150 °C, conversion: 59%, see Table S5, Entry 11).

4.3 Semilogarithmic Plots for the Determination of k_{app}

4.3.1 General Remarks on the Analysis of Polymerization Kinetics

All polymerization experiments were monitored by *in-situ* Raman spectroscopy. The interval of the recording ranged from 15 s to 1 min depending on the polymerization rate. The integral of the lactide (LA) modes (624–713 cm^{-1}) was used for the determination of the conversion p by comparing the current integral of the lactide mode $Int(LA)_t$ at time t with the integral at the beginning of the polymerization $Int(LA)_0$ (t = 0 s):

$$p = 1 - \frac{\mathrm{Int}(LA)_t}{\mathrm{Int}(LA)_0}$$

For pseudo first order reaction kinetics the apparent rate constant k_{app} is determined by plotting ln(1/(1-p)) (= $\ln(Int(LA)_0/Int(LA)_t)$ versus t. In the following, all semilogarithmic plots of the polymerization experiments from Tables S5–S9 are depicted (see Section 4.1). The initial k_{app} values were determined from the initial data points that are in accordance with a linear fit. All data points considered for the linear regression are depicted in blue color and points that were not considered are in gray color. The regression line is displayed in red color. The time range used for the linear regression, the regression line equation and the coefficient of determination (R^2) are indicated at the plots.

The experiments conducted without any catalyst (see Table S5 Entries 19–20 and Fig. S40) indicate that even when no catalyst is applied an initial increase of the conversion p is observable. The ^{1}H NMR spectrum of these experiments shows no conversion after 5 h at 150 °C. Therefore, the observed initial increase is not due to a polymerization but to the melting of lactide until it is equally distributed in the reactor. However, this affects only experiments with low polymerization rates caused by high [M]/[I] ratios or low catalyst activities. For these experiments, the first three data points collected were omitted for the determination of the linear regression. Moreover, for the experiments conducted without catalyst fluctuations on ln(1/(1-p)) in the range of ±0.02 [a. u.] occurred. This effect is mainly visible for polymerizations with very low polymerization rates.

During some experiments, saturation effects occurred due to a dark coloration of the polymer melt. This led to a plateau-like region in the plot. The respective data points were neglected.

4.3.2 Screening of Catalysts (Table S5)

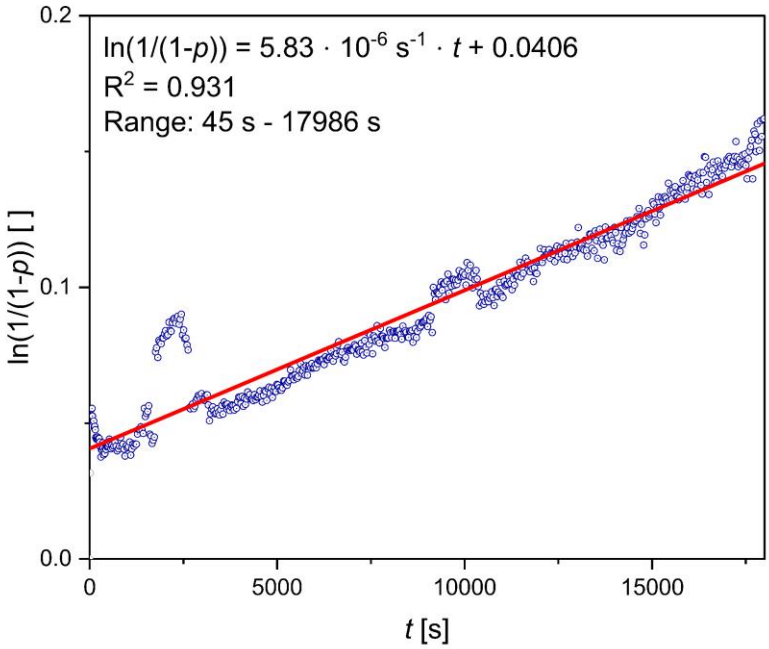

Fig. S22: Semilogarithmic plot for the polymerization of recrystallized L-lactide with [Fe(TMG$_2$b)Cl$_2$] / [Fe(TMG$_2$b)Cl$_2$]·1.5MeCN (**C1**/**C1**·1.5MeCN) ([LLA]/[**C1**] = 1000:1, 150 °C, 5 h, see Table S5 Entry 1). The exact [M]/[I] ratio is not known since the complex can crystallize as an acetonitrile solvate and the synthesis was not selective. The [M]/[I] ratio was calculated for the acetonitrile-free species **C1**. The fluctuations found in the plot are normal for experiments with low polymerization rates that are close to the signal-to-noise limit.

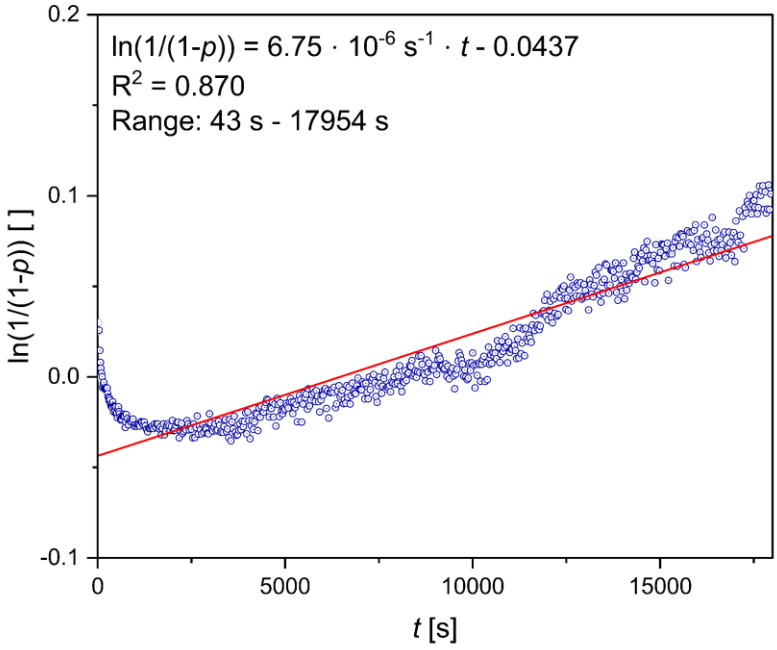

Fig. S23: Semilogarithmic plot for the polymerization of recrystallized L-lactide with [Fe(TMG$_2$b)Cl$_2$] (**C1**)/ [Fe(TMG$_2$b)Cl$_2$]·1.5MeCN (**C1**·1.5MeCN) ([LLA]/[**C1**] = 1000:1, 150 °C, 5 h, see Table S5 Entry 2). The accurate [M]/[I] ratio is not known since the complex can crystallize as an acetonitrile solvate and the synthesis was not selective. The fluctuations found in the plot are normal for experiments with low polymerization rates that are close to the signal-to-noise limit.

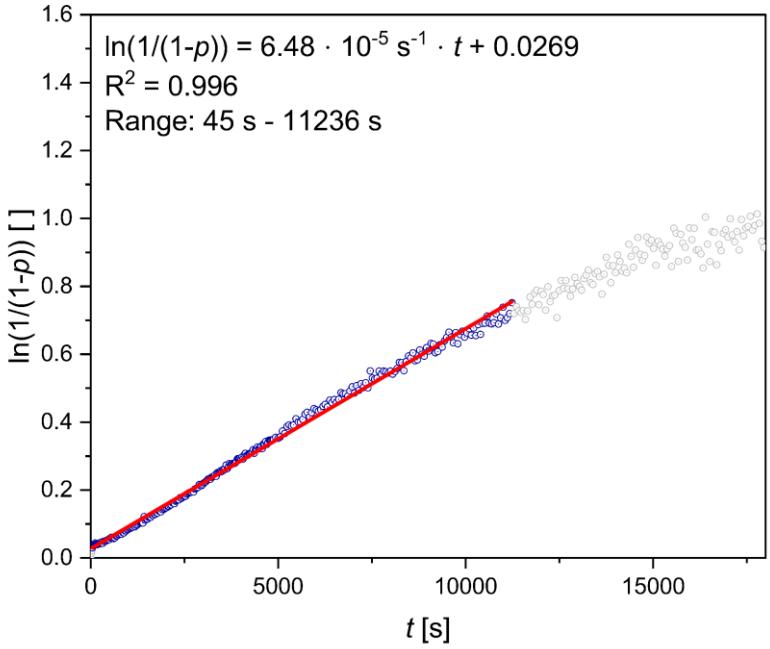

Fig. S24: Semilogarithmic plot for the polymerization of recrystallized L-lactide with [Fe(TMG$_2$n)Cl$_2$] (**C2**) ([LLA]/[**C2**] = 1000:1, 150 °C, 5 h, Table S5 Entry 3).

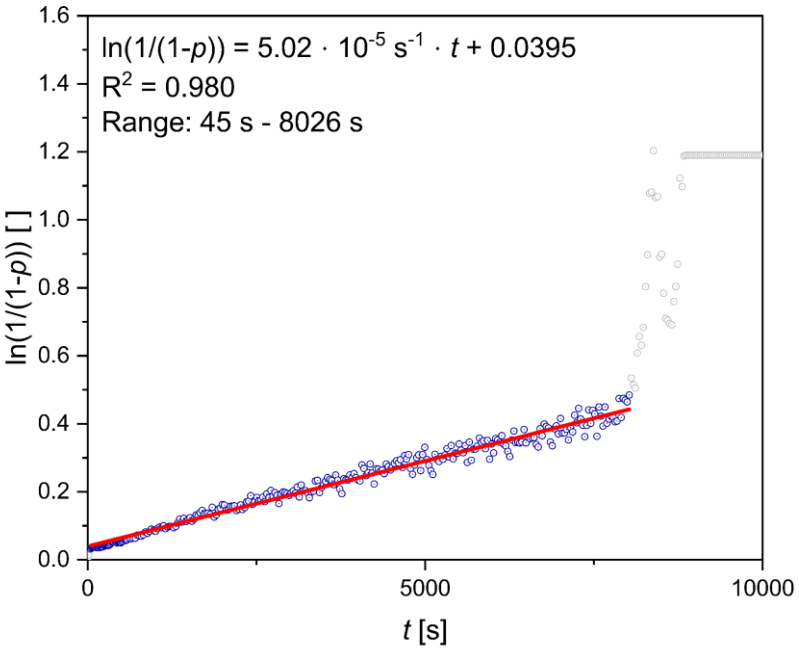

Fig. S25: Semilogarithmic plot for the polymerization of recrystallized L-lactide with [Fe(TMG$_2$n)Cl$_2$] (**C2**) ([LLA]/[**C2**] = 1000:1, 150 °C, 5 h, Table S5, Entry 4). The fluctuations found in the plot are due to saturation effects caused by the dark coloration of the reaction mixture.

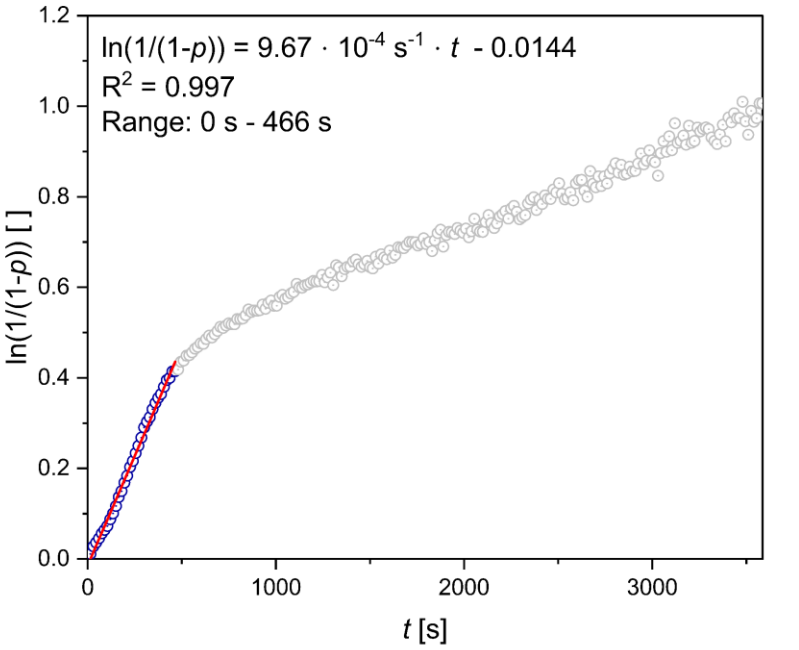

Fig. S26: Semilogarithmic plot for the polymerization of recrystallized L-lactide with [Fe(TMG$_2$e)Cl$_2$] (**C3**) ([LLA]/[**C3**] = 1000:1, 150 °C, 1 h, see Table S5 Entry 5).

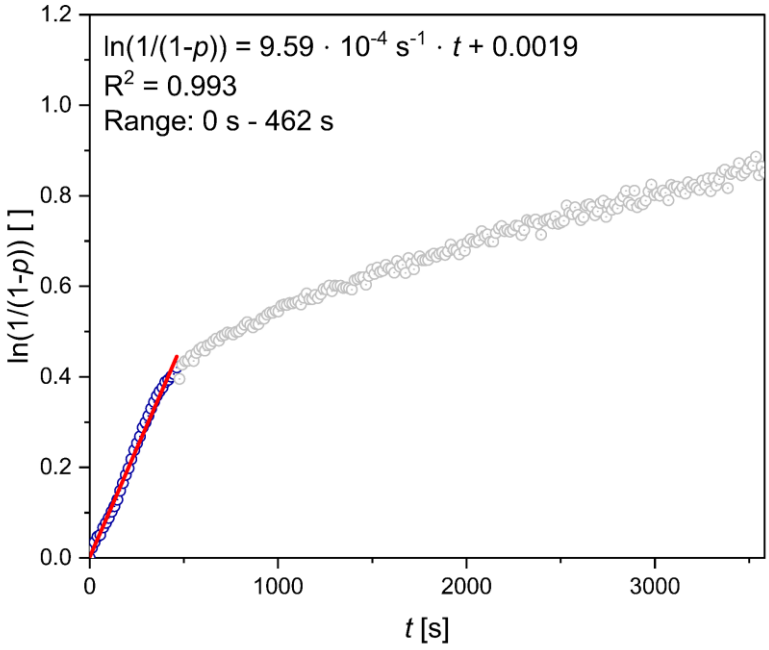

Fig. S27: Semilogarithmic plot for the polymerization of recrystallized L-lactide with [Fe(TMG$_2$e)Cl$_2$] (**C3**) ([LLA]/[**C3**] = 1000:1, 150 °C, 1 h, see Table S5 Entry 6).

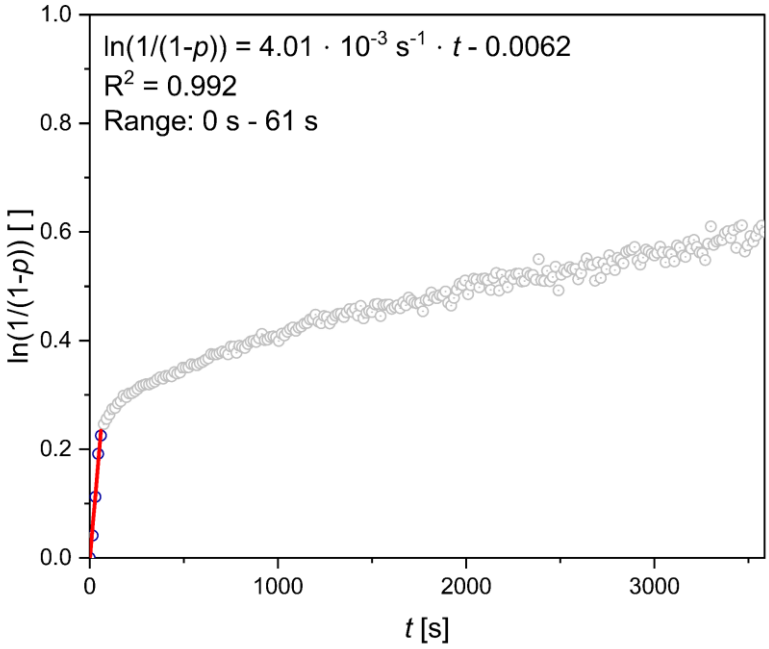

Fig. S28: Semilogarithmic plot for the polymerization of recrystallized L-lactide with [Fe(TMG$_2$p)Cl$_2$] (**C4**) ([LLA]/[**C4**] = 1000:1, 150 °C, 1 h, see Table S5 Entry 7).

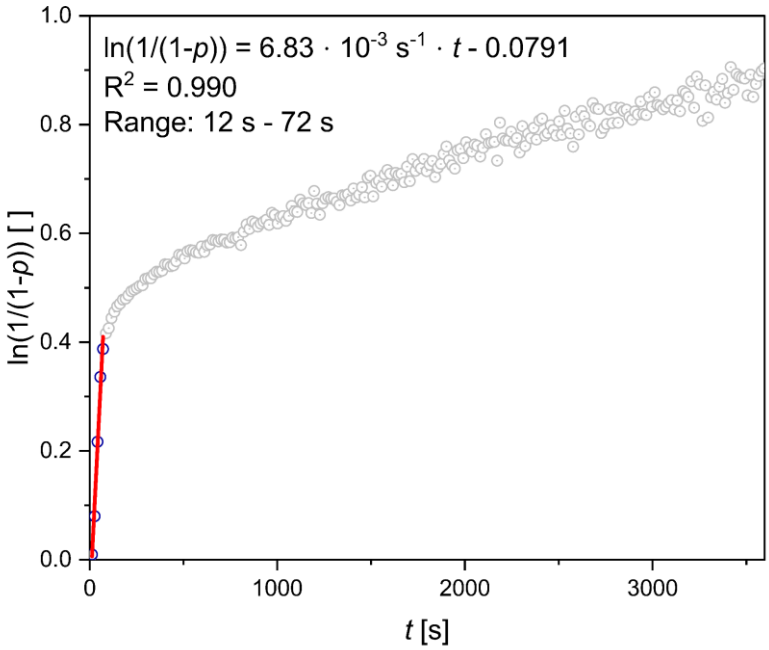

Fig. S29: Semilogarithmic plot for the polymerization of recrystallized L-lactide with [Fe(TMG$_2$p)Cl$_2$] (**C4**) ([LLA]/[**C4**] = 1000:1, 150 °C, 1 h, see Table S5 Entry 8).

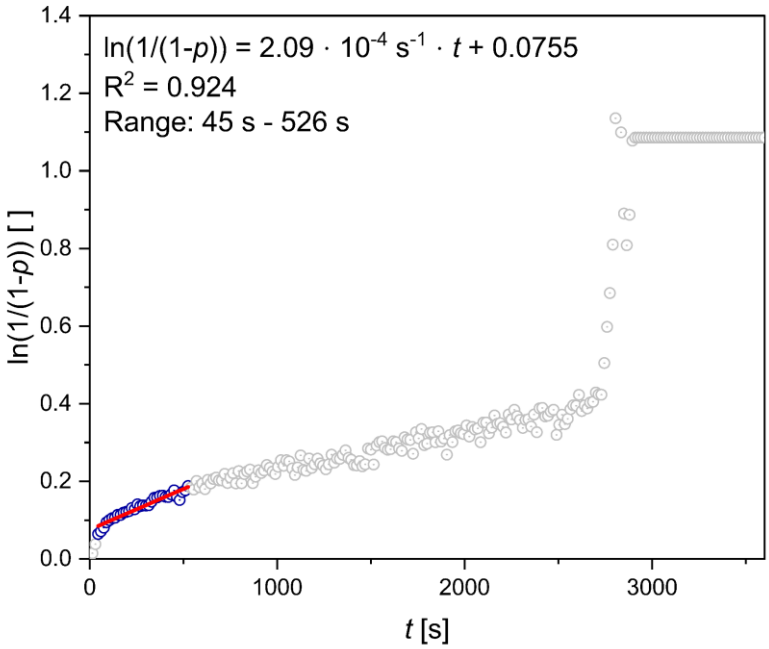

Fig. S30: Semilogarithmic plot for the polymerization of recrystallized L-lactide with [Fe(TMGpy)$_2$Cl]Cl (**C5**) ([LLA]/[**C5**] = 1000:1, 150 °C, 1 h, see Table S5 Entry 9). The fluctuations found in the plot are due to saturation effects caused by the dark coloration of the reaction mixture.

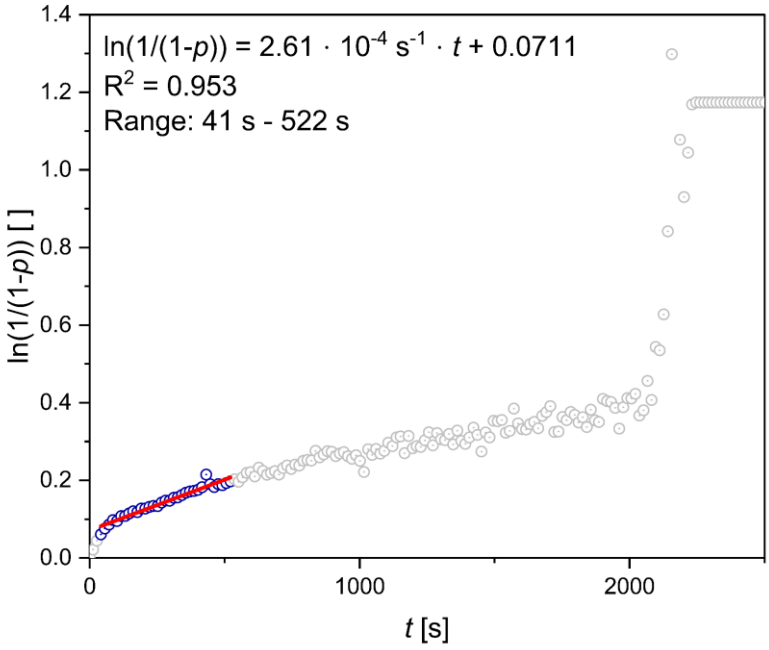

Fig. S31: Semilogarithmic plot for the polymerization of recrystallized L-lactide with [Fe(TMGpy)$_2$Cl]Cl (**C5**) ([LLA]/[**C5**] = 1000:1, 150 °C, 1 h, see Table S5 Entry 10). The fluctuations found in the plot are due to saturation effects caused by the dark coloration of the reaction mixture.

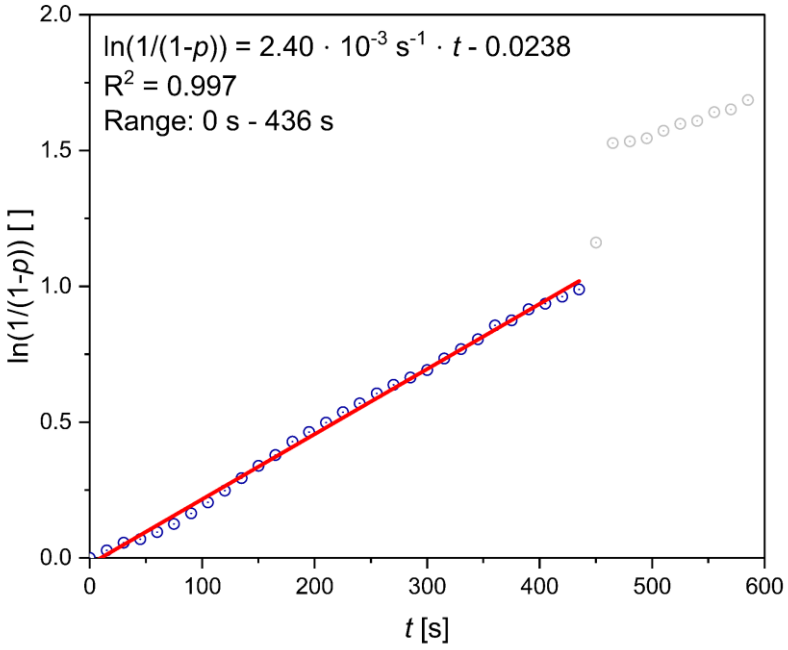

Fig. S32: Semilogarithmic plot for the polymerization of recrystallized L-lactide with [Fe(TMGepy)Cl$_2$] (**C6**) ([LLA]/[**C6**] = 1000:1, 150 °C, 10 min, see Table S5 Entry 11). The discontinuity at the end of the measurement is due to the high viscosity of the polymer melt and the resulting limited mixing.

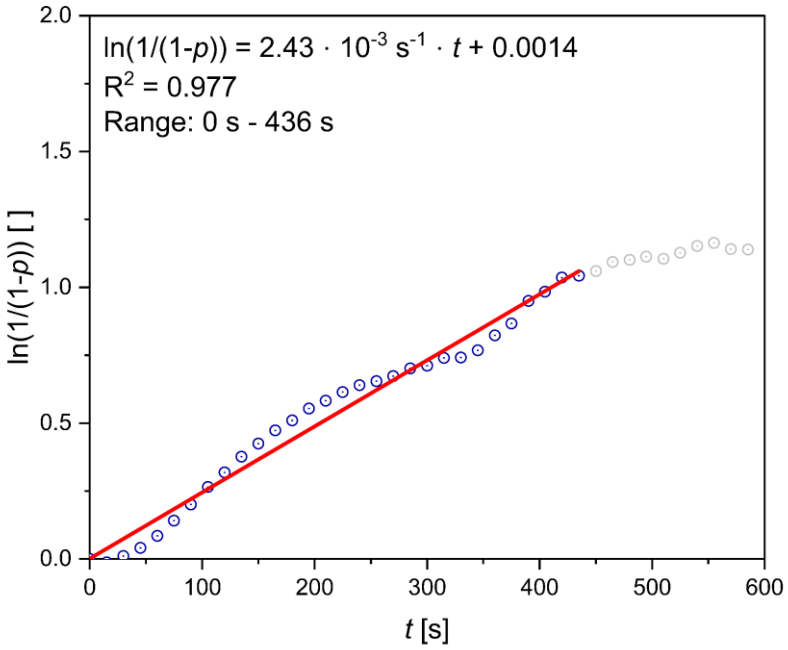

Fig. S33: Semilogarithmic plot for the polymerization of recrystallized L-lactide with [Fe(TMGepy)Cl_2] (**C6**) ([LLA]/[**C6**] = 1000:1, 150 °C, 10 min, see Table S5 Entry 12).

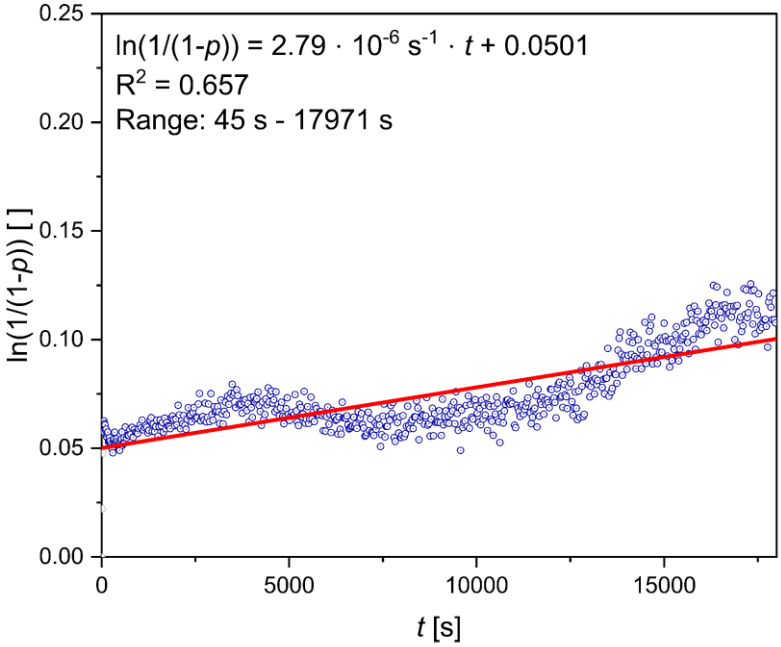

Fig. S34: Semilogarithmic plot for the polymerization of recrystallized L-lactide with [Fe(DMEG$_2$b)Cl_2] (**C7**) ([LLA]/[**C7**] = 1000:1, 150 °C, 5 h, see Table S5 Entry 13). The experiment shows a very low polymerization rate and the recorded data is close to the signal-to-noise limit.

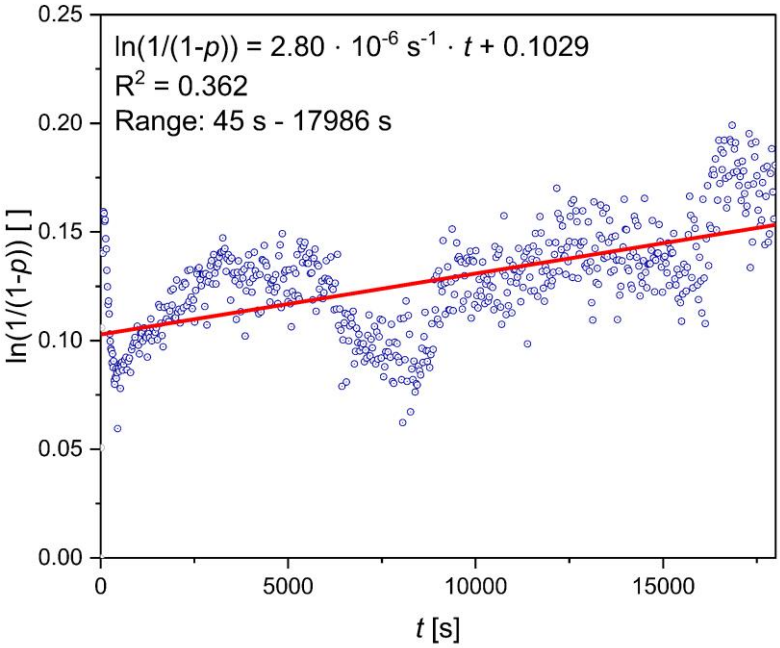

Fig. S35: Semilogarithmic plot for the polymerization of recrystallized L-lactide with [Fe(DMEG$_2$b)Cl$_2$] (**C7**) ([LLA]/[**C7**] = 1000:1, 150 °C, 5 h, see Table S5 Entry 14). The experiment shows a very low polymerization rate and the recorded data is close to the signal-to-noise limit.

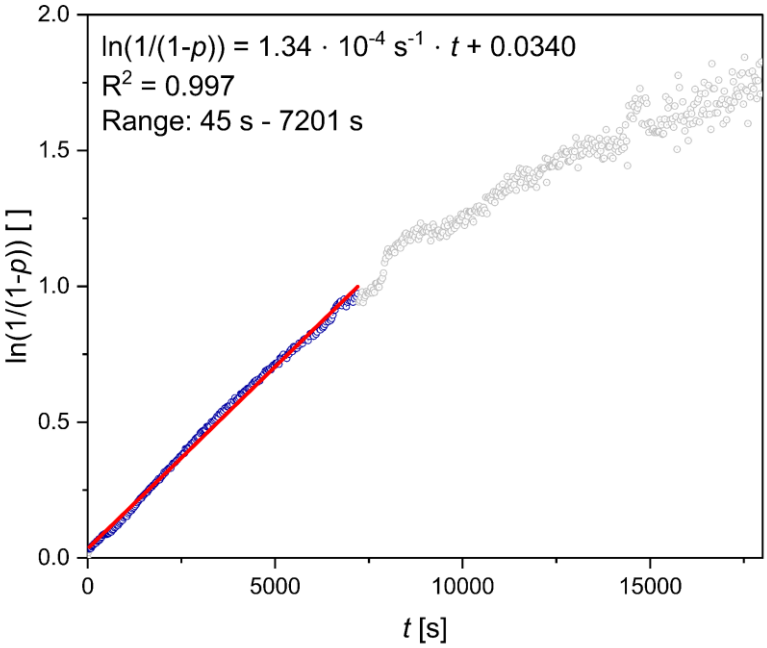

Fig. S36: Semilogarithmic plot for the polymerization of recrystallized L-lactide with [Fe(DMEG$_2$n)Cl$_2$] (**C8**) ([LLA]/[**C8**] = 1000:1, 150 °C, 5 h, see Table S5 Entry 15).

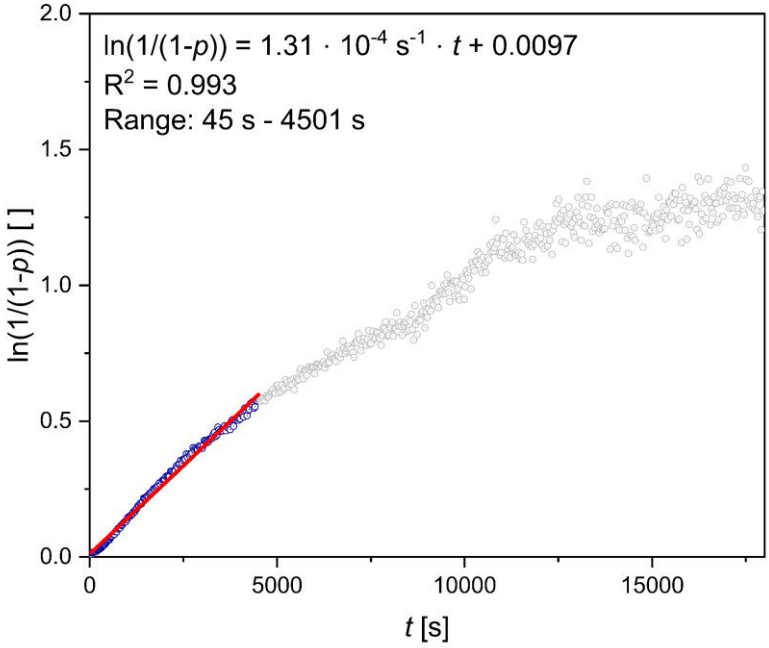

Fig. S37: Semilogarithmic plot for the polymerization of recrystallized L-lactide with [Fe(DMEG$_2$n)Cl$_2$] (**C8**) ([LLA]/[**C8**] = 1000:1, 150 °C, 5 h, see Table S5 Entry 16)

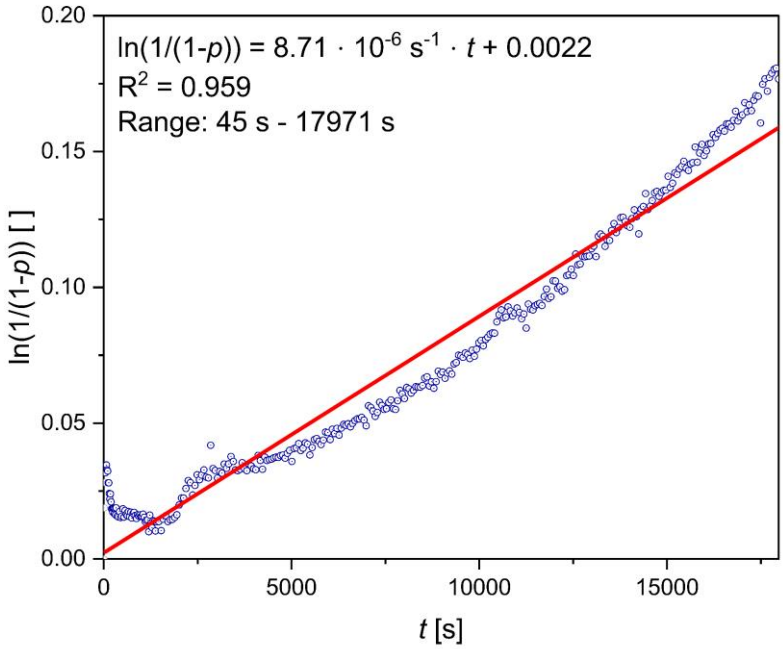

Fig. S38: Semilogarithmic plot for the polymerization of recrystallized L-lactide with $FeCl_2$ ([LLA]/[$FeCl_2$] = 1000:1, 150 °C, 5 h, see Table S5 Entry 17). The experiment shows a very low polymerization rate and the recorded data is close to the signal-to-noise limit.

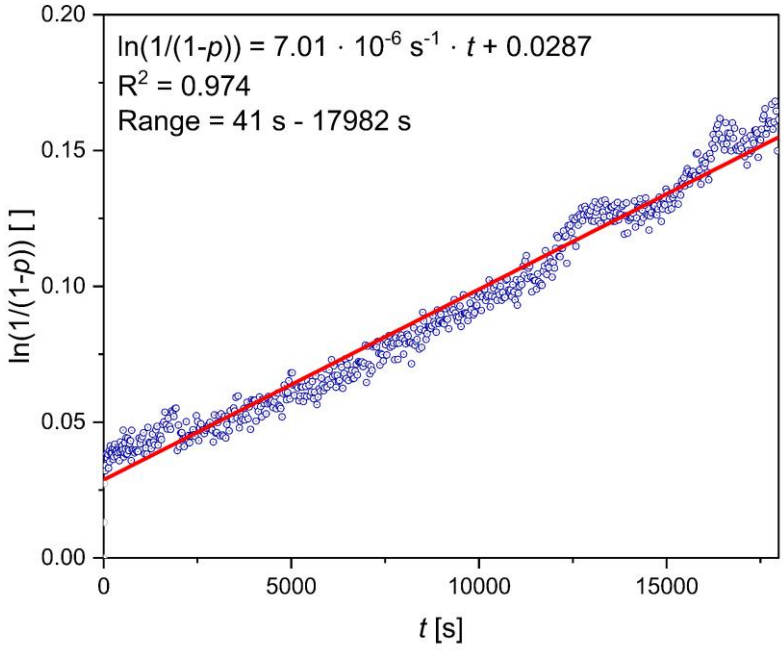

Fig. S39: Semilogarithmic plot for the polymerization of recrystallized L-lactide with $FeCl_2$ ([LLA]/[$FeCl_2$] = 1000:1, 150 °C, 5 h, see Table S5 Entry 18). The experiment shows a very low polymerization rate and the recorded data is close to the signal-to-noise limit.

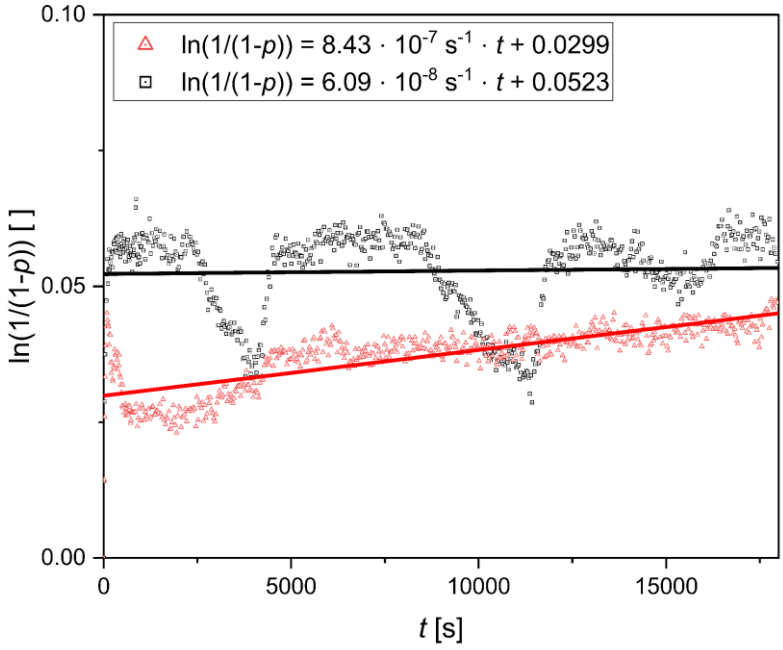

Fig. S40: Semilogarithmic plot of the experiments without catalyst (only recrystallized L-lactide, 150 °C, 5 h, see Table S5 Entries 19 and 20). Both plots exhibit fluctuations and show slopes lower than $1 \cdot 10^{-6}$ s^{-1} indicating that k_{app} values below $1 \cdot 10^{-6}$ s^{-1} are in general negligible. Fluctuations of ln(1/(1-*p*)) in the range of ±0.02 [a.u.] are inevitable. An initial increase of the apparent conversion is even observed for pure L-lactide which is due to the melting of lactide. However, this is not due to polymerization as proven by the ^{1}H NMR spectrum.

4.3.3 Additional Polymerization Experiments with [Fe(TMG$_2$e)Cl$_2$] (C3) (Table S6)

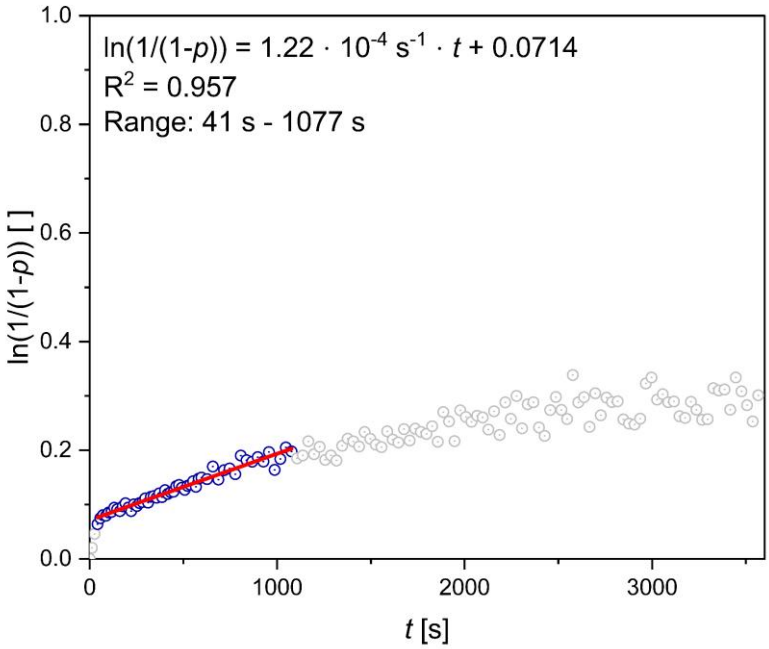

Fig. S41: Semilogarithmic plot for the polymerization of recrystallized L-lactide with $FeCl_2$ and TMG_2e (**L3**) ([LLA]/[$FeCl_2$]/[TMG_2e] = 1000:1:1, 150 °C, 1 h, see Table S6 Entry 1).

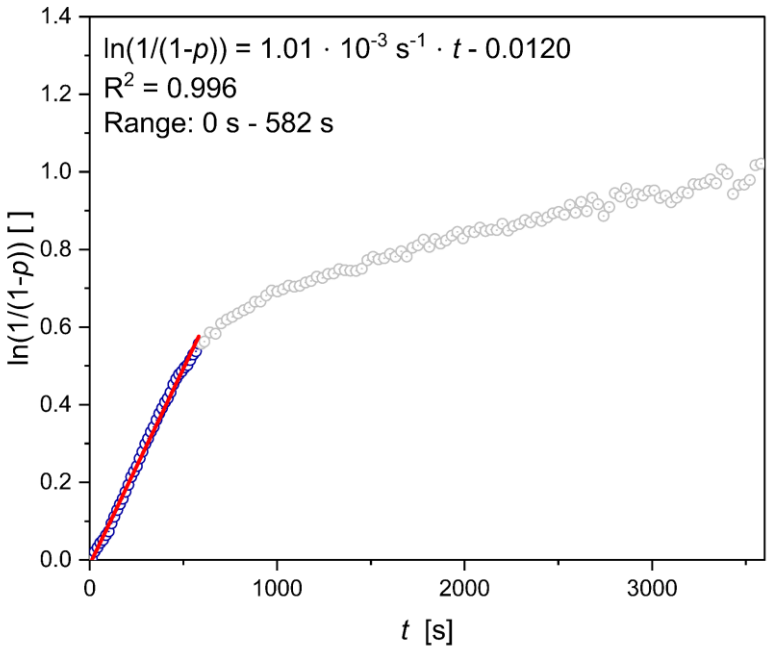

Fig. S42: Semilogarithmic plot for the polymerization of recrystallized L-lactide with [Fe(TMG$_2$e)Cl$_2$] (**C3**) and para-methyl benzyl alcohol ([LLA]/[**C3**]/[*p*MeBnOH] = 1000:1:1, 150 °C, 1 h, see Table S6 Entry 2).

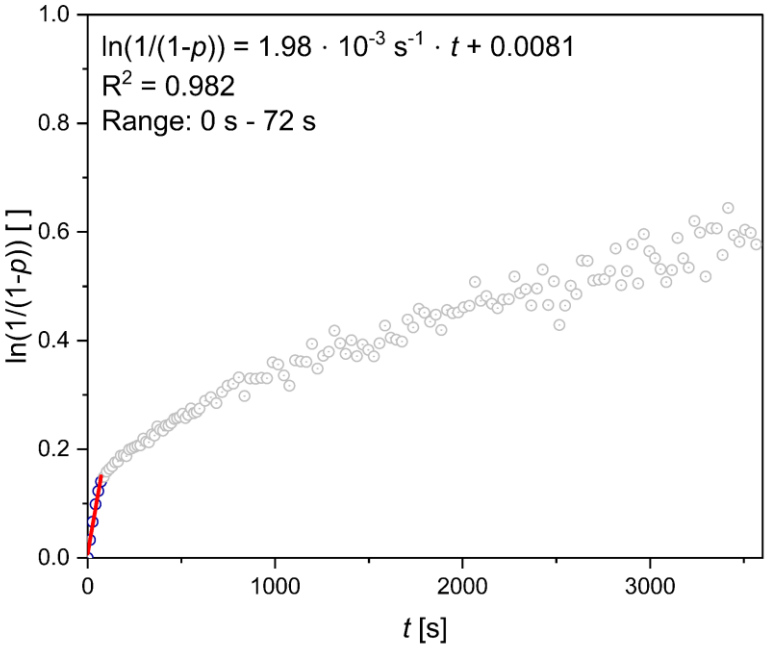

Fig. S43: Semilogarithmic plot for the polymerization of recrystallized L-lactide with [Fe(TMG$_2$e)Cl$_2$] (**C3**) and TMG$_2$e ([LLA]/[**C3**]/[TMG$_2$e] = 1000:1:1, 150 °C, 1 h, see Table S6 Entry 3).

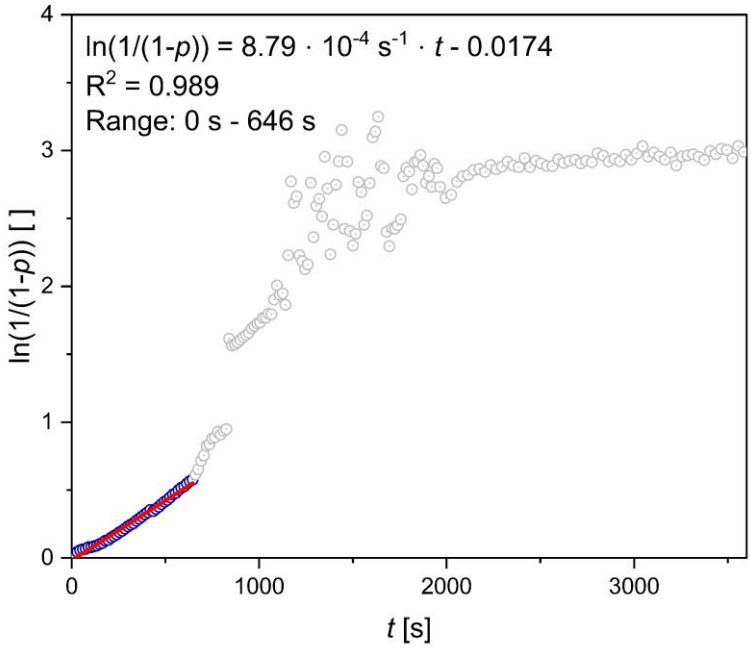

Fig. S44: Semilogarithmic plot for the polymerization of recrystallized L-lactide with [Fe(TMG$_2$e)Cl$_2$] (**C3**) and FeCl$_2$ ([LLA]/[**C3**]/[FeCl$_2$] = 1000:1:1, 150 °C, 1 h, see Table S6 Entry 4). The fluctuations are due to the high viscosity of the polymer melt and the resulting limited mixing.

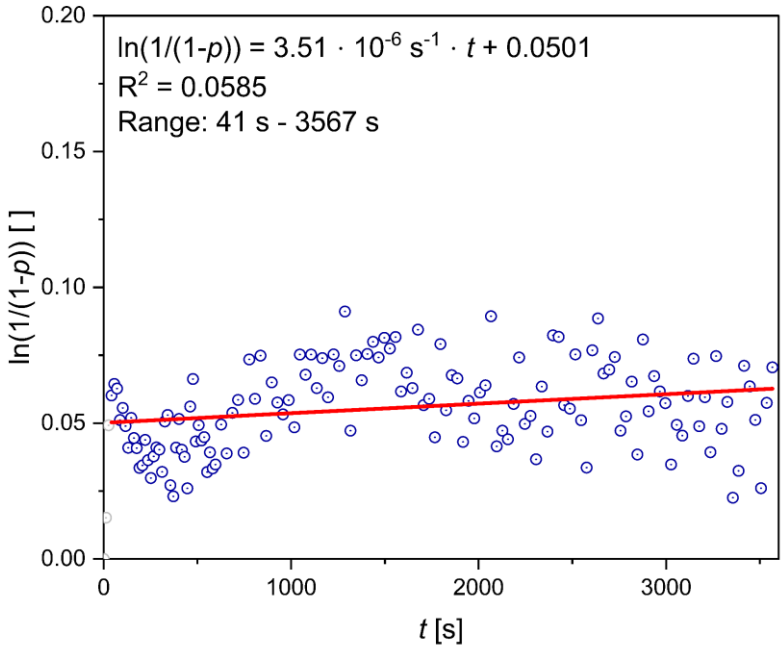

Fig. S45: Semilogarithmic plot for the polymerization of recrystallized L-lactide with ligand TMG_2e (**L3**)([LLA]/[TMG_2e] = 1000:1, 150 °C, 1 h, see Table S6 Entry 5). The plot shows strong fluctuations of the conversion and can only be analyzed inaccurately which is due to a low conversion of only 11% after 1 h as determined by ^1H NMR.

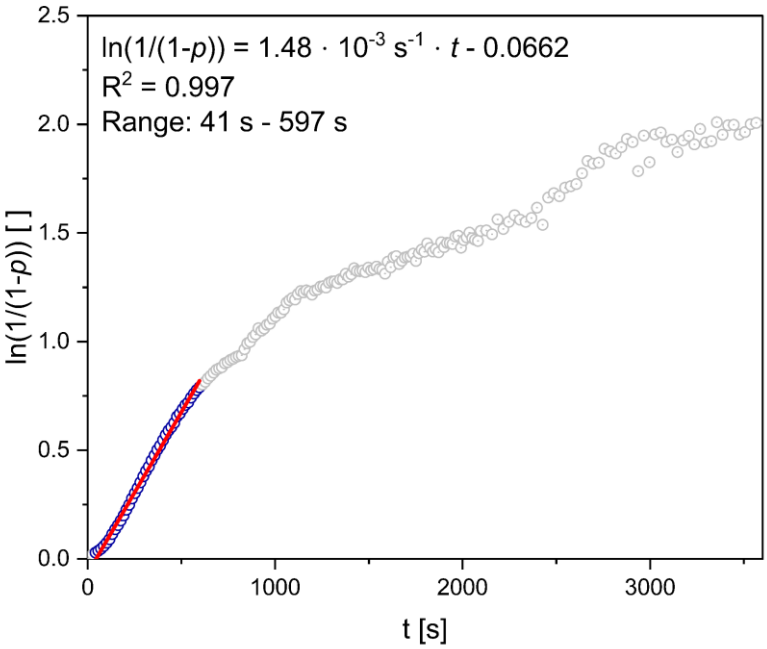

Fig. S46: Semilogarithmic plot for the polymerization of recrystallized L-lactide with [Fe(TMG_2e)Cl_2] (**C3**) ([LLA]/[**C3**] = 500:1, 150 °C, 1 h, see Table S6 Entry 6)

4.3.4 Polymerization Experiments for the k_p Determination for [Fe(TMGepy)Cl_2] (C6) (Table S7)

The concentration-independent rate constant k_p was determined by plotting the k_{app} values versus the catalyst concentration (see main paper). The catalyst concentration [**C6**] was calculated using the density of liquid lactide at 150 °C (δ(LA, 150 °C) = 1.138 g mL^{-1}) as given in literature [35]. The semilogarithmic plots for the determination of the initial k_{app} values at different catalyst concentrations are displayed in Fig. S32 and S33 ([LLA]/[**C6**] = 1000:1) and S47–S51 ([LLA]/[**C6**] = 1250:1, 1500:1, 2000:1 and 5000:1). For [LLA]/[**C6**] ratios of 1500:1 and higher, the first data points were omitted because the increase due to the melting of lactide surpasses the reaction rate and would therefore distort the determined initial k_{app} values (see Fig. S40). Both end points ([LLA]/[**C6**] ratios of 1000:1 and 5000:1) were determined in duplicate.

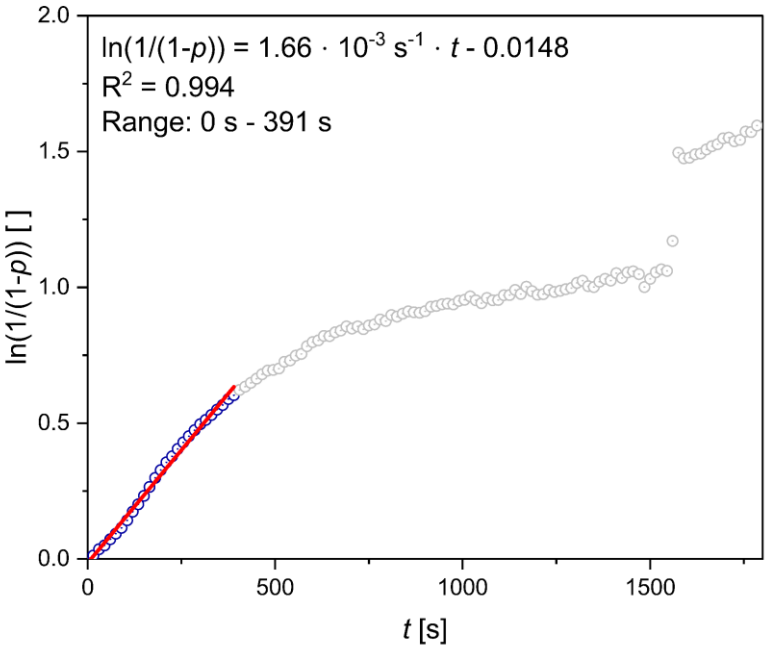

Fig. S47: Semilogarithmic plot for the polymerization of recrystallized L-lactide with [Fe(TMGepy)Cl_2] (**C6**) ([LLA]/[**C6**] = 1250:1, 150 °C, 30 min, see Table S7 Entry 3). The discontinuity of the plot is caused by the high viscosity of the polymerization mixture and the resulting limited mixing.

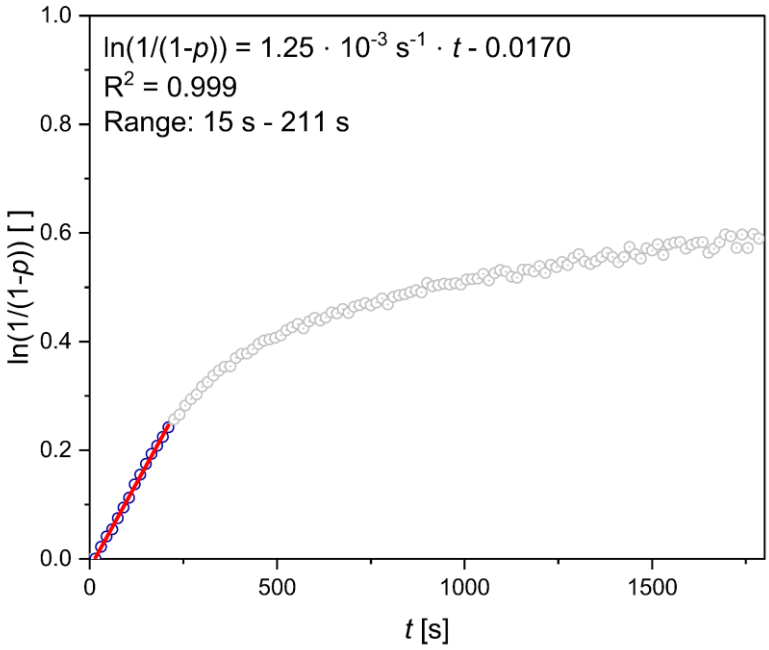

Fig. S48: Semilogarithmic plot for the polymerization of recrystallized L-lactide with [Fe(TMGepy)Cl_2] (**C6**) ([LLA]/[**C6**] = 1500:1, 150 °C, 30 min, see Table S7 Entry 4).

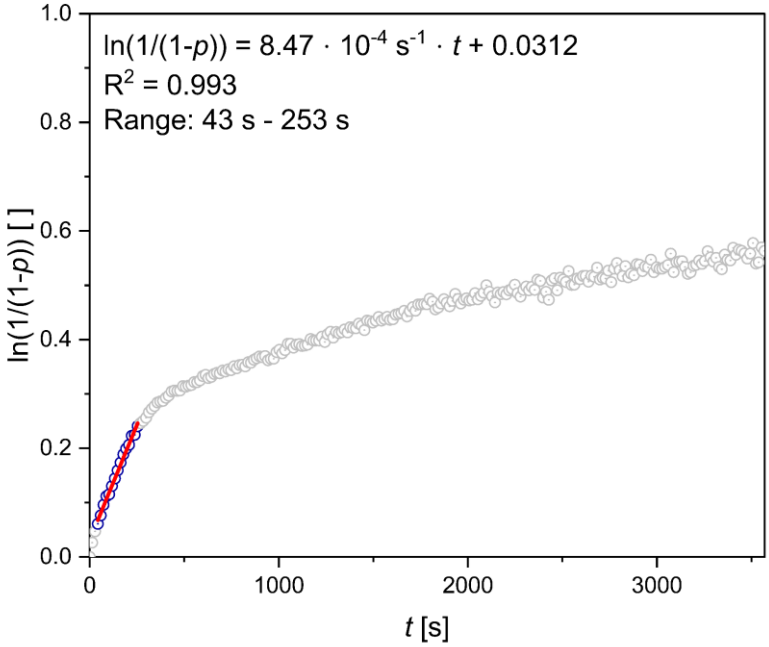

Fig. S49: Semilogarithmic plot for the polymerization of recrystallized L-lactide with [Fe(TMGepy)Cl_2] (**C6**) ([LLA]/[**C6**] = 2000:1, 150 °C, 60 min, see Table S7 Entry 5).

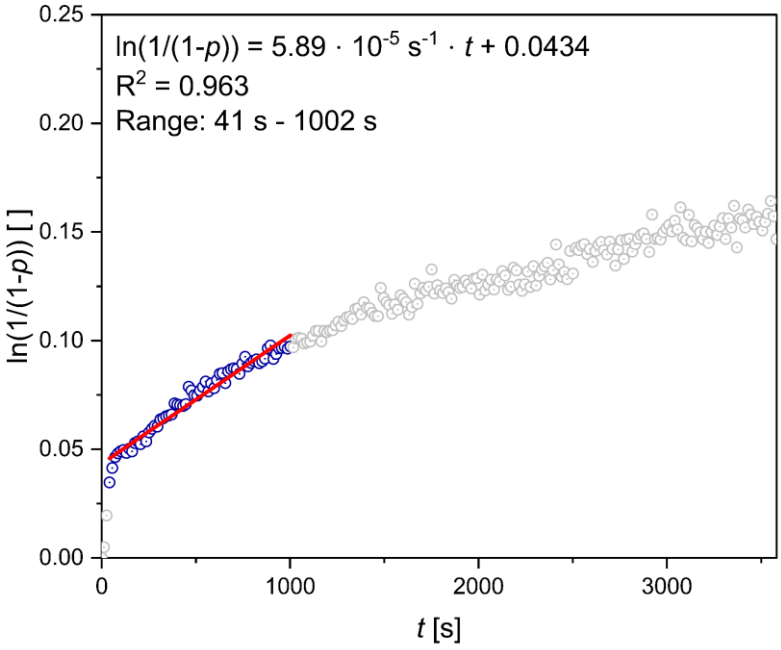

Fig. S50: Semilogarithmic plot for the polymerization of recrystallized L-lactide with [Fe(TMGepy)Cl_2] (**C6**) ([LLA]/[**C6**] = 5000:1, 150 °C, 60 min, see Table S7 Entry 6).

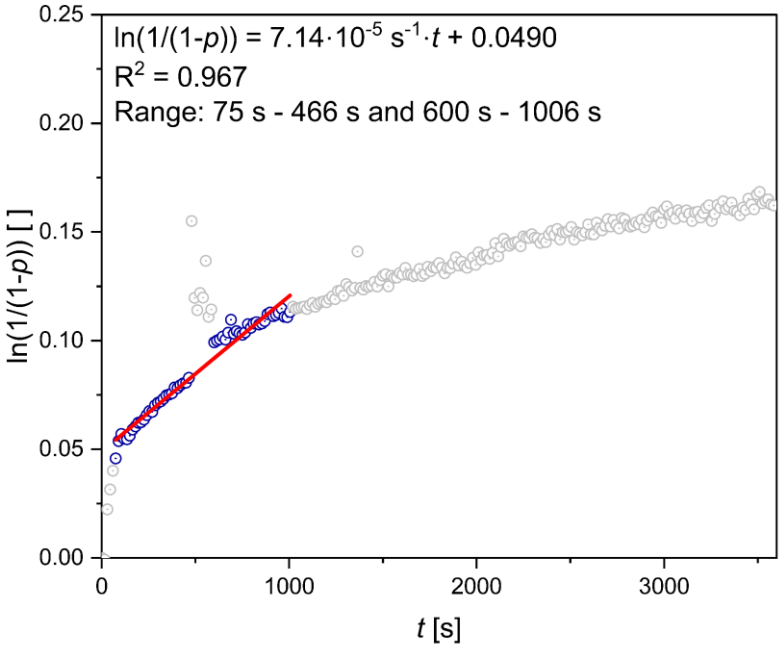

Fig. S51: Semilogarithmic plot for the polymerization of recrystallized L-lactide with [Fe(TMGepy)Cl_2] (**C6**) ([LLA]/[**C6**] = 5000:1, 150 °C, 60 min, see Table S7 Entry 7). The fluctuations between 466 s and 600 s are likely due to uneven mixing of the melt. Therefore, strongly deviating points were neglected for the linear regression.

4.3.5 Additional Polymerization Experiments with C4 and C6 at Different Temperatures and Varying Lactide Purities (Table S8)

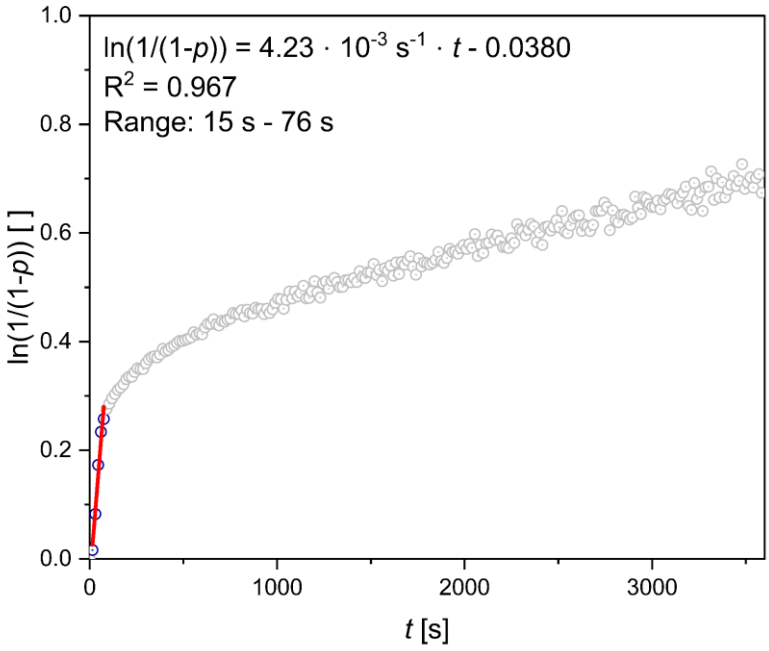

Fig. S52: Semilogarithmic plot for the polymerization of sublimated L-lactide with [Fe(TMG$_2$p)Cl$_2$] (**C4**) ([LLA]/[**C4**] = 1000:1, 150 °C, 1 h, see Table S8, Entry 1).

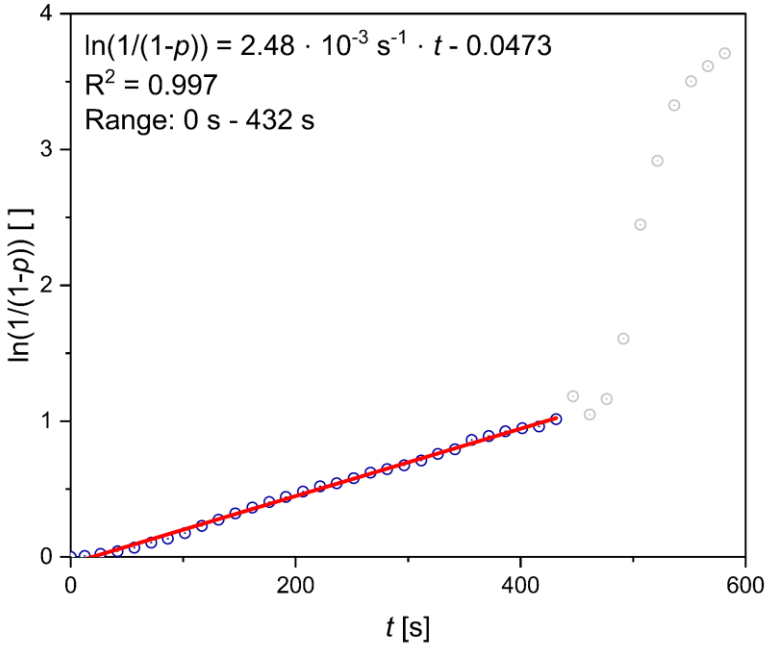

Fig. S53: Semilogarithmic plot for the polymerization of sublimated L-lactide with [Fe(TMGepy)Cl$_2$] (**C6**) ([LLA]/[**C6**] = 1000:1, 150 °C, 10 min, see Table S8 Entry 2). The fast increase after 432 s is due to the high viscosity of the polymer melt and uneven mixing.

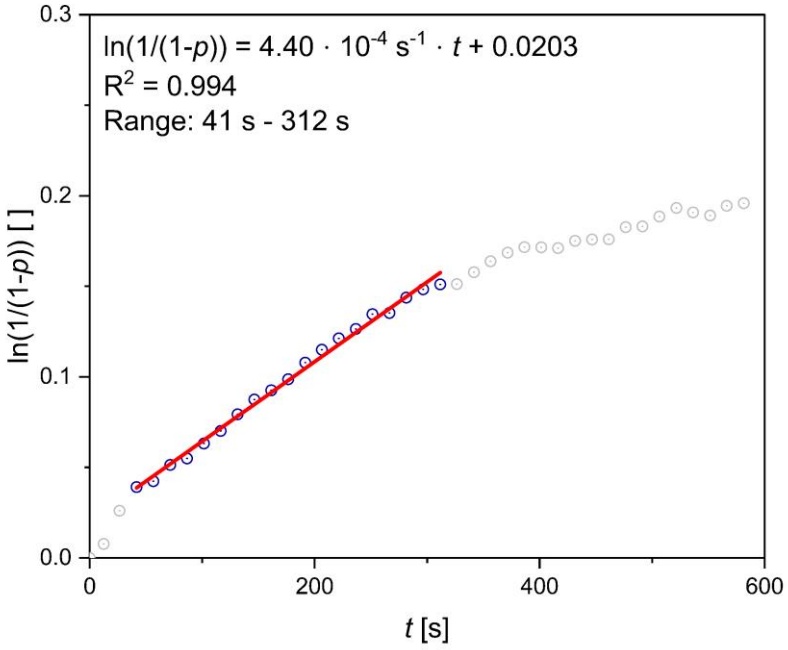

Fig. S54: Semilogarithmic plot for the polymerization of recrystallized L-lactide with [Fe(TMGepy)Cl_2] (**C6**) ([M]/[I] = 1000:1, 135 °C, 10 min, see Table S8 Entry 3).

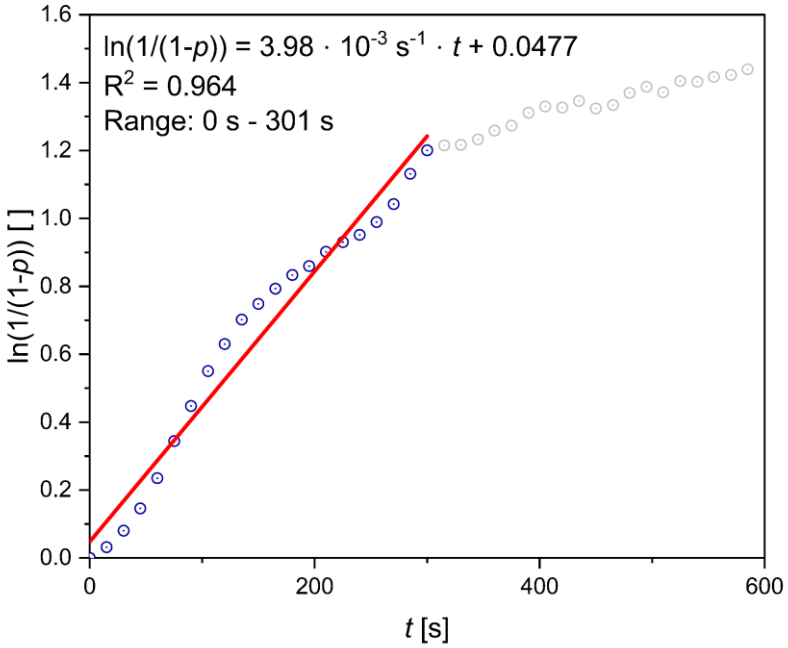

Fig. S55: Semilogarithmic plot for the polymerization of recrystallized L-lactide with [Fe(TMGepy)Cl_2] (**C6**) ([LLA]/[**C6**] = 1000:1, 180 °C, 10 min, see Table S8 Entry 4).

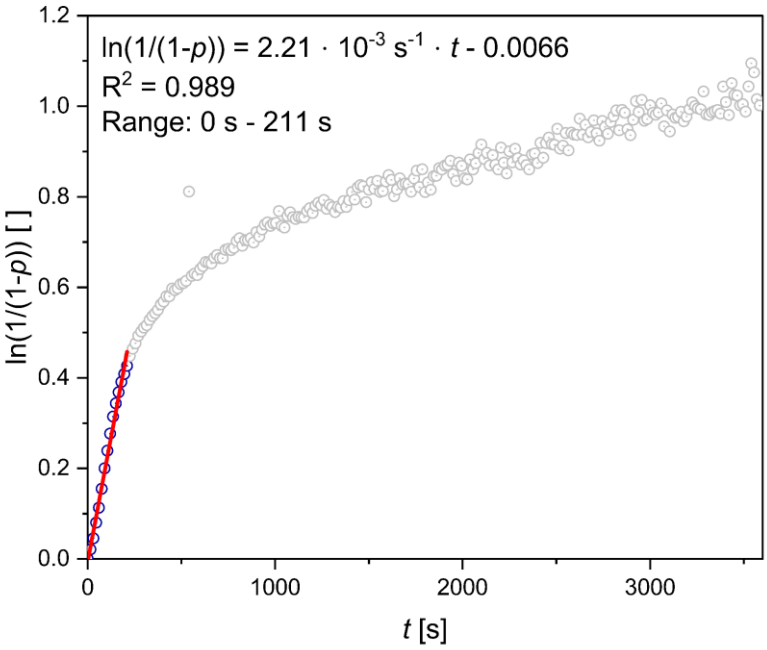

Fig. S56: Semilogarithmic plot for the polymerization of recrystallized L-lactide with [Fe(TMGepy)Cl_2] (**C6**) ([LLA]/[**C6**] = 2000:1, 180 °C, 10 min, see Table S8 Entry 5).

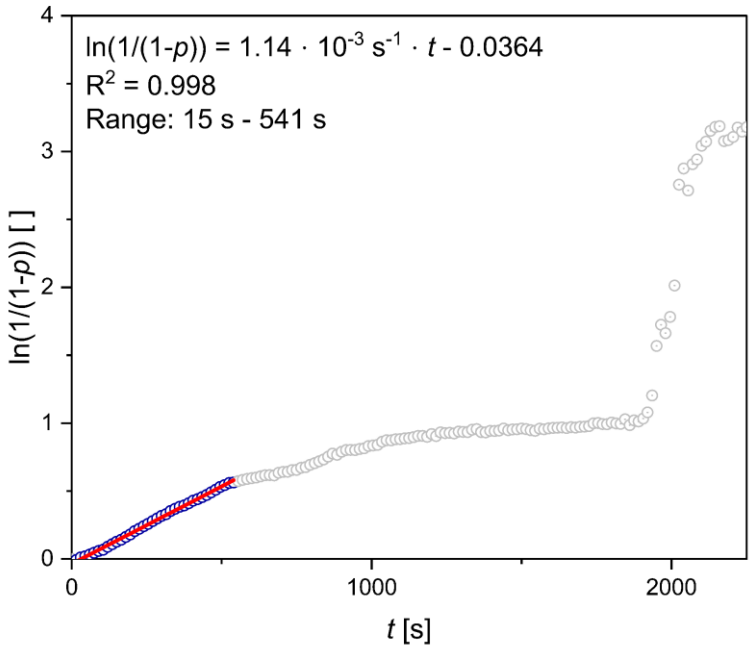

Fig. S57: Semilogarithmic plot for the polymerization of sublimated L-lactide with [Fe(TMGepy)Cl_2] (**C6**) ([LLA]/[**C6**] = 2000:1, 150 °C, 1 h, see Table S8 Entry 6). The discontinuity is due to the high viscosity of the polymerization mixture and the resulting limited mixing.

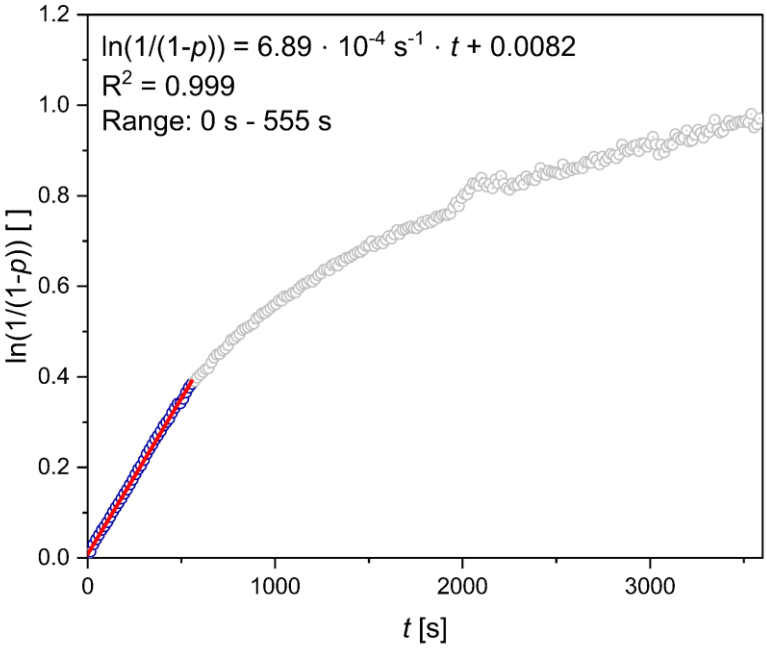

Fig. S58: Semilogarithmic plot for the polymerization of technical-grade *rac*-lactide with [Fe(TMGepy)Cl_2] (**C6**) ([*rac*-LA]/[**C6**] = 2000:1, 150 °C, 1 h, see Table S8 Entry 7).

4.3.6 Polymerization Experiments with C6 and Co-Initiator (Table S9)

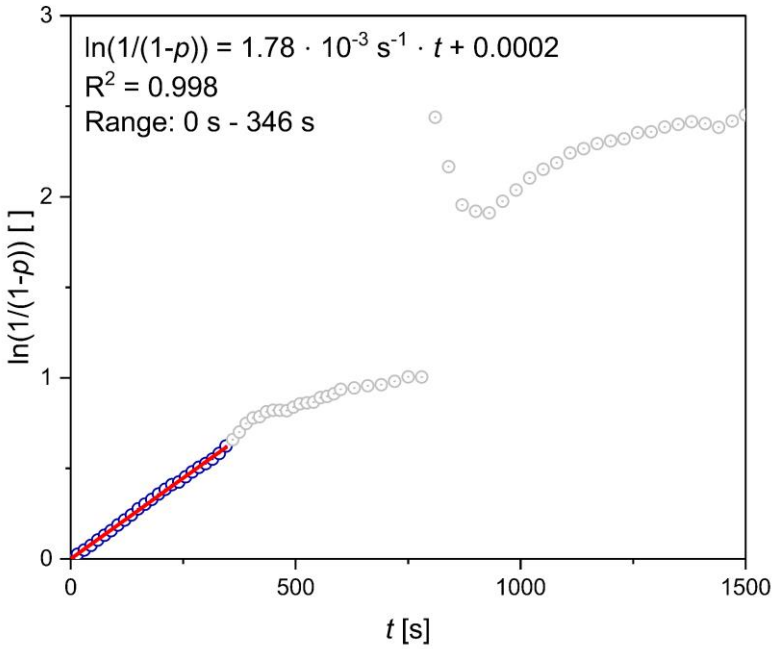

Fig. S59: Semilogarithmic plot for the polymerization of recrystallized L-lactide with [Fe(TMGepy)Cl_2] (**C6**) and co-initiator para-methyl benzyl alcohol ([LLA]/[**C6**]/[*p*MeBnOH] = 2000:1:1, 150 °C, 1 h, see Table S9 Entry 1). The discontinuity and the fluctuations are due to the high viscosity of the polymer melt and the resulting limited mixing.

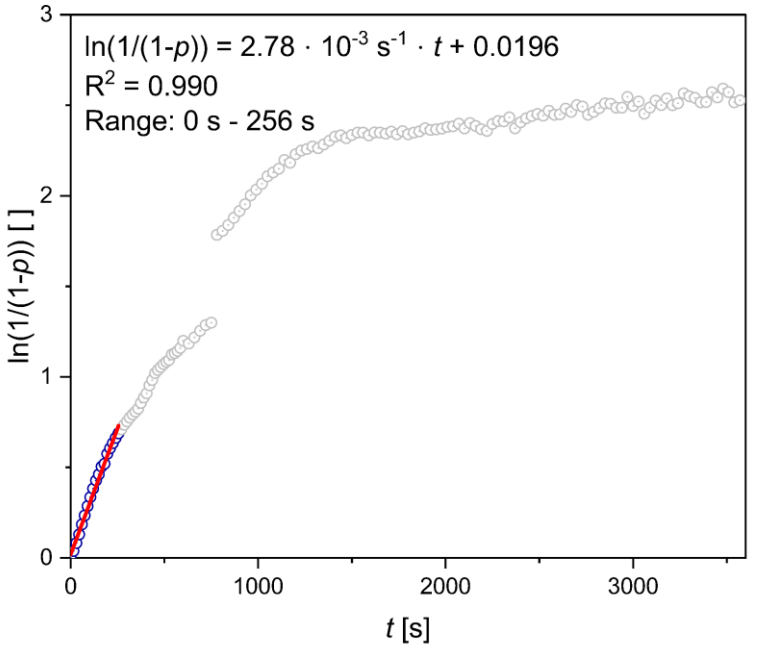

Fig. S60: Semilogarithmic plot for the polymerization of recrystallized L-lactide with [Fe(TMGepy)Cl_2] (**C6**) and co-initiator para-methyl benzyl alcohol ([LLA]/[**C6**]/[*p*MeBnOH] = 2000:1:4, 150 °C, 1 h, see Table S9

Entry 2). The discontinuity is due to the high viscosity of the polymerization mixture and the resulting limited mixing.

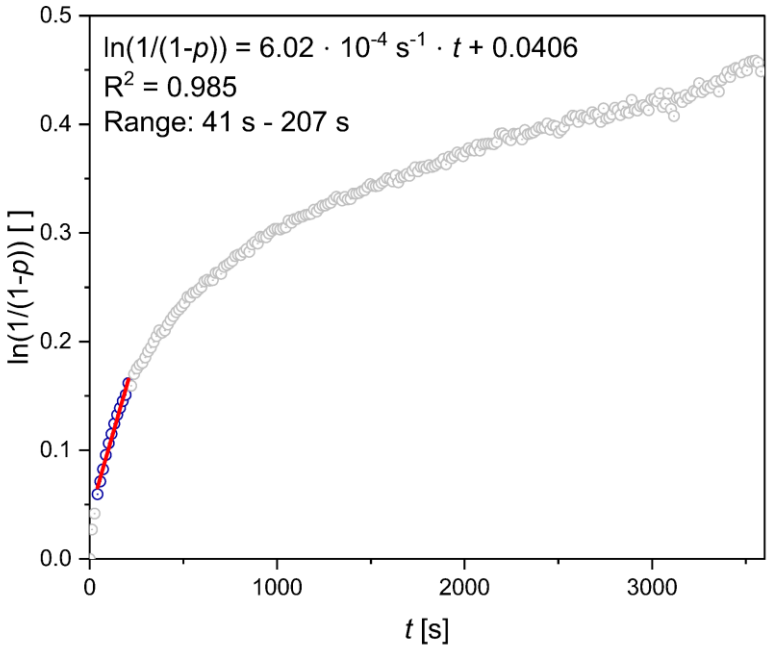

Fig. S61: Semilogarithmic plot for the polymerization of recrystallized L-lactide with [Fe(TMGepy)Cl_2] (**C6**) and co-initiator para-methyl benzyl alcohol ([LLA]/[**C6**]/[*p*MeBnOH] = 5000:1:5, 150 °C, 1 h, see Table S9 Entry 3).

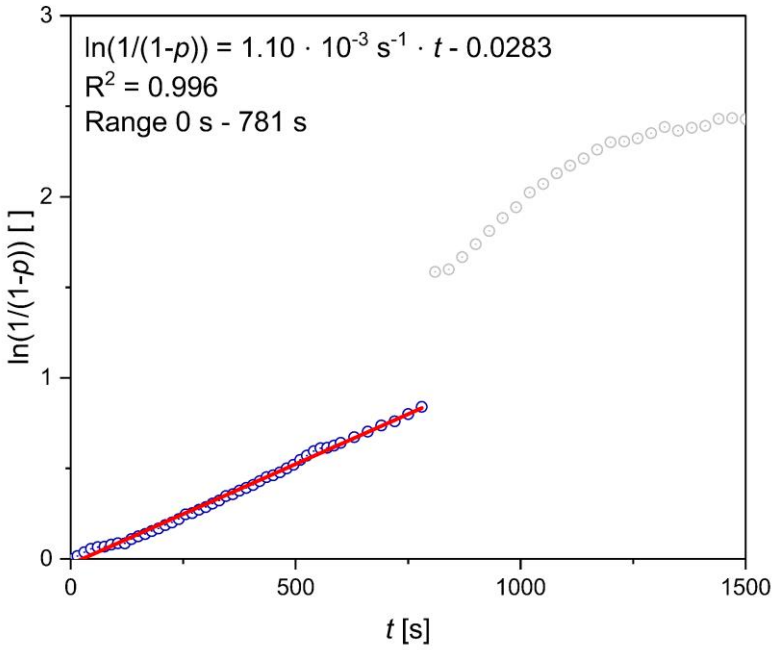

Fig. S62: Semilogarithmic plot for the polymerization of recrystallized L-lactide with [Fe(TMGepy)Cl_2] (**C6**) and $FeCl_2$ ([LLA]/[**C6**]/[$FeCl_2$] = 2000:1:1, 150 °C, 1 h, see Table S9 Entry 4). The discontinuity and the strong fluctuations are due to the high viscosity of the reaction mixture and the resulting limited mixing.

5 DSC

Table S10: DSC Results for PLA synthesized with [Fe(TMGepy)Cl_2] (**C6**).[a]

No.	Experiment (Section 4.1)	[LLA]/[**C6**]/[*p*MeBnOH]	T_g [°C][b]	T_m [°C]	ΔH_m [J·g^{-1}]	Fig.
1	Table S5 Entry 11	1000/1/–	59.1	172.7	38.00	S63
2	Table S9 Entry 1	2000/1/1	61.4	171.4	42.67	S64
3	Table S9 Entry 2	2000/1/4	61.2	169.4	38.54	S65

[a] Determined from the second heating/cooling cycle. [b] Inflection point.

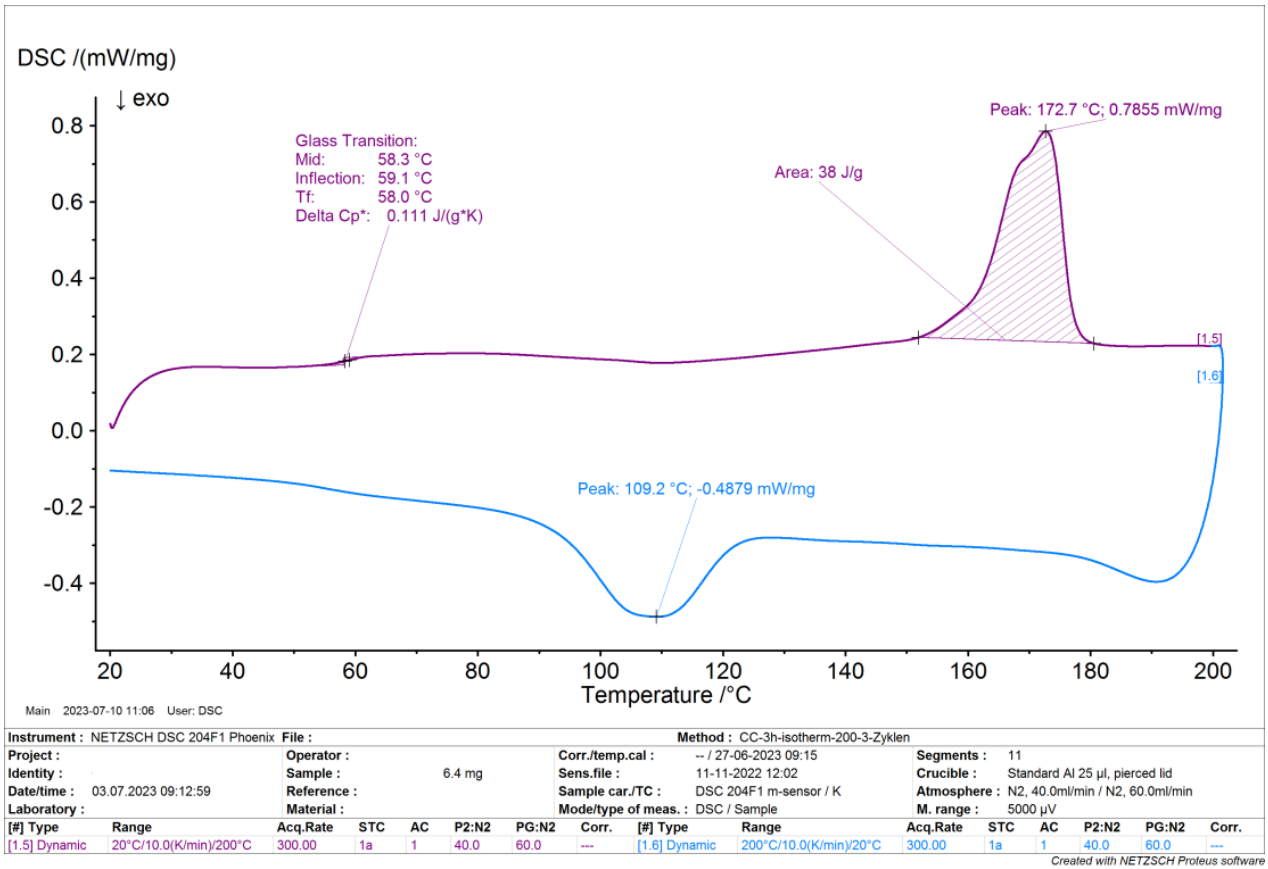

Fig. S63: DSC results for PLA synthesized with [Fe(TMGepy)Cl_2] (**C6**, [LLA]/[**C6**] = 1000:1, 150 °C, 1 h, see Table S5 Entry 11). The second heating/cooling cycle is depicted.

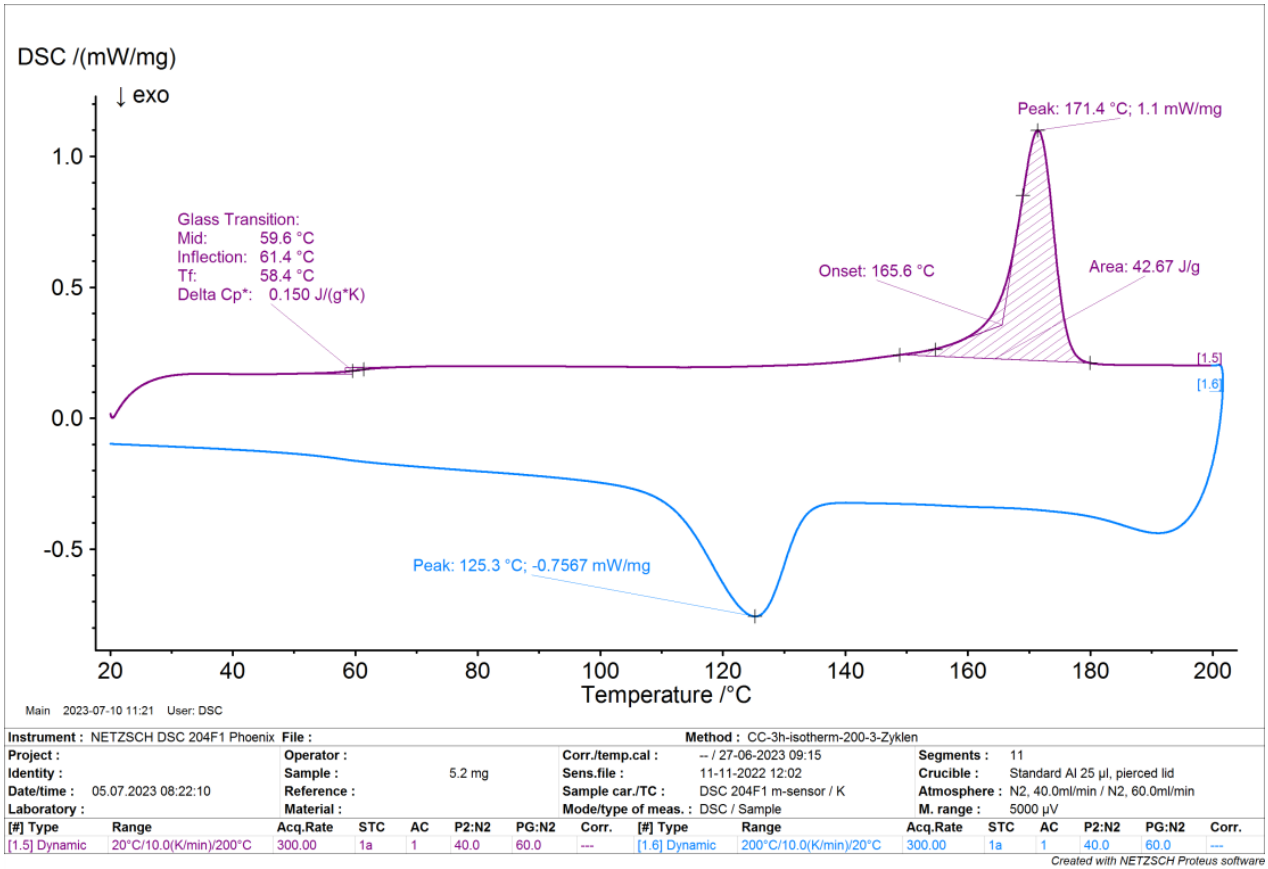

Fig. S64: DSC results for PLA synthesized with [Fe(TMGepy)Cl_2] (**C6**) and co-initiator *p*MeBnOH ([LLA]/[**C6**]/[*p*MeBnOH] = 2000:1:1, 150 °C, 1 h, see Table S9 Entry 1). The second heating/cooling cycle is depicted.

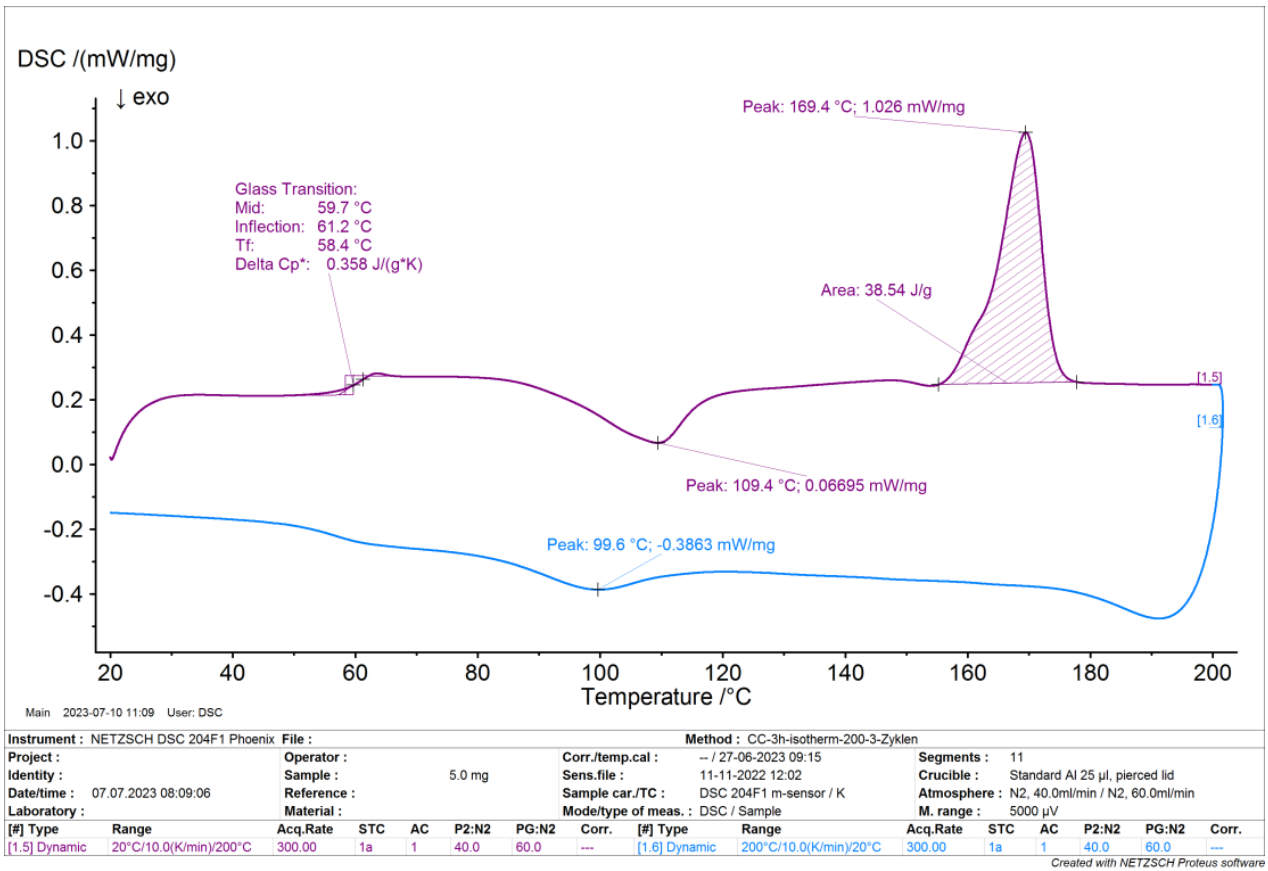

Fig. S65: DSC results for PLA synthesized with [Fe(TMGepy)Cl_2] (**C6**) and co-initiator *p*MeBnOH ([LLA]/[**C6**]/[*p*MeBnOH] = 2000:1:4, 150 °C, 1 h, see Table S9 Entry 2). The second heating/cooling cycle is depicted.

6 MALDI-TOF-MS End Group Analysis

6.1 Preparation of MALDI-TOF-MS Samples

Inside a nitrogen-filled glovebox, recrystallized L-lactide (600 mg, 4.16 mmol, 100 equiv), the catalyst **C6** (14.5 mg, 0.0416 mmol, 1.00 equiv) and, if appropriate, *p*MeBnOH (5.1 mg, 0.042 mmol, 1.0 equiv) were homogenized in a mortar for 10 min. The mixture was transferred to a Schlenk-tube, the tube was sealed with a Young-type lid and removed from the glovebox. Then, the tube was immerged into an oil-bath pre-heated to 150 °C. After the desired reaction time, the Schlenk tube was cooled under a stream of cold water. The polymer was dissolved in DCM (2 mL) and removed from the Schlenk tube. The solvent was subsequently removed under reduced pressure and a sample (5–6 mg) for the MALDI-TOF-MS measurement was taken. In total, two samples were prepared (see Table S11).

Table S11: Polymerization experiments conducted for the MALDI-TOF-MS samples.[a]

No.	[LLA]/[**C6**]/[*p*MeBnOH]	*t* [min]	*p* [%]
1	100/1/–	5	90
2	100/1/1	5	100

[a] Conditions: stirred Schlenk tube, recrystallized LLA, 150 °C.

6.2 MALDI-TOF-MS Spectra

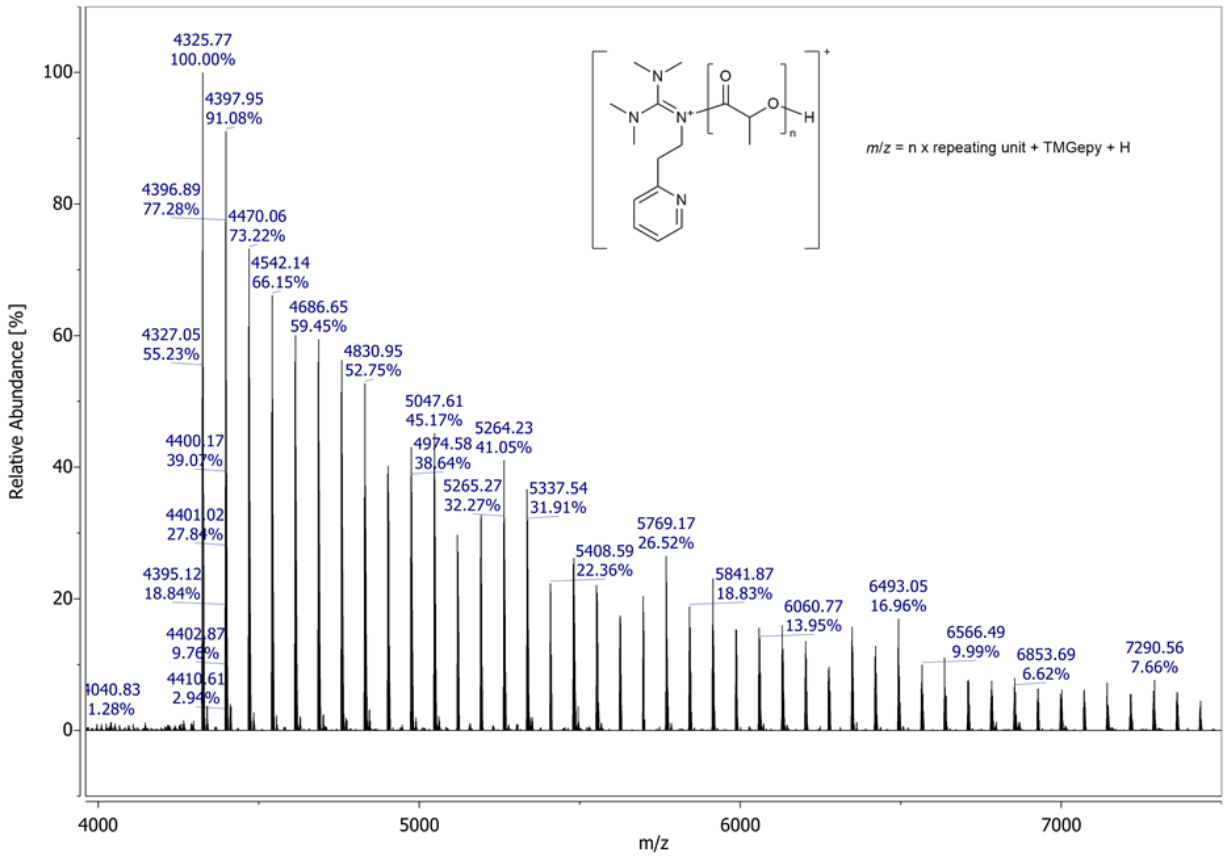

Fig. S66: Excerpt of the MALDI-TOF-MS spectrum of the polymerization of recrystallized L-lactide with [Fe(TMGepy)Cl_2] (**C6**) (Stirred Schlenk-tube, [LLA]/[**C6**] = 100:1, *T* = 150 °C, *t* = 5 min). Example calculation: 4686 = 62 × repeating unit + TMGepy + H.

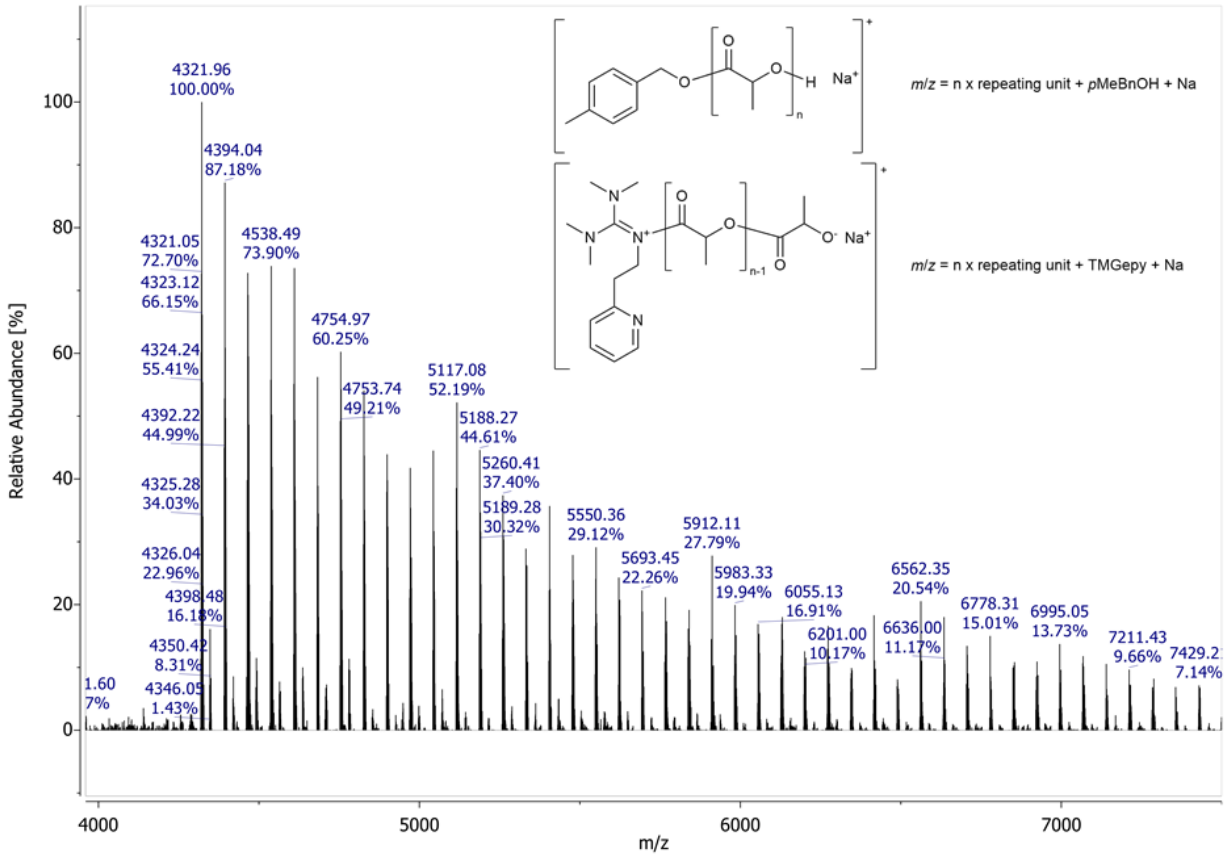

Fig. S67: Excerpt of the MALDI-TOF-MS spectrum of the polymerization of recrystallized L-lactide with [Fe(TMGepy)Cl_2] (**C6**) and the co-initiator *p*-methyl benzyl alcohol (Stirred Schlenk-tube, [LLA]/[**C6**]/[*p*MeBnOH] = 100:1:1, T = 150 °C, t = 5 min). Example calculation: 4394 = 59 × repeating unit + *p*MeBnOH + Na.

Table S12: Results of MALDI-TOF-MS end group analysis for the polymerization with **C6**.

end group	without co-initiator (Fig. S66)	with co-initiator (Fig. S67)
TMGepy (ligand)	yes	yes
*p*MeBnOH (co-initiator)	no	yes
OH	yes	no

7 Methanolysis of PLA

Table S13: Depolymerization experiments.[a]

Entry	Complex	t [min]	X_{int}[b] [%]	$S_{Me\text{-}LA}$[b] [%]	$Y_{Me\text{-}LA}$[b] [%]	k_{app}[c] [min^{-1}]	Fig.
1	**C2**	1440	13	5	1	n.d.[d]	
2	**C2**	1440	69	52	36	n.d.[d]	
3	**C2**	1440	26	19	5	n.d.[d]	
4	**C3**	180	98	82	80	0.0235	S68
5	**C3**	180	99	88	87	0.0291	S68
6	**C3**	180	100	93	93	0.0265	S68
7	**C4**	180	99	89	88	0.0296	S69
8	**C4**	180	99	82	81	0.0315	S69
9	**C5**	15	100	100	100	n. d.[e]	
10	**C5**	15	100	100	100	n. d.[e]	
11	**C6**	186	67	43	29	0.0045	S70
12	**C6**	180	67	42	28	0.0054	S70
13[f]	$FeCl_2$	360	4	0	0	n. d.	
14[f]	$FeCl_2$	1320	21	21	4	n. d.	

[a] Conditions: 250 mg PLA film (bio-mi Ltd., M_n = 46.7 kg mol^{-1}, M_w/M_n = 1.5), 1 mol% catalyst (regarding the PLA ester bonds), methanol (7.13 equiv.), THF (4 mL), T = 60 °C, stirring speed: 260 rpm. [b] The conversion of internal methine groups of PLA (X_{int}), the selectivity towards the product methyl lactate (S_{MeLa}) and the yield of the product (Y_{MeLa}) were calculated from the ^{1}H NMR spectra according to literature.[36] [c] Determined from the plot of $\ln([Int]_0/[Int]_t)$ vs. t. Average value with standard deviation is given. [d] The depolymerization proceeds very slow and the semilogarithmic plot is not in good accordance with a pseudo first order reaction. Therefore, k_{app} was not determined. [e] The depolymerization proceeds very fast. Therefore, no k_{app} value could be determined. [f] Entries 13 and 14 are the same experiment. The number of data points was not sufficient for the determination of k_{app}.

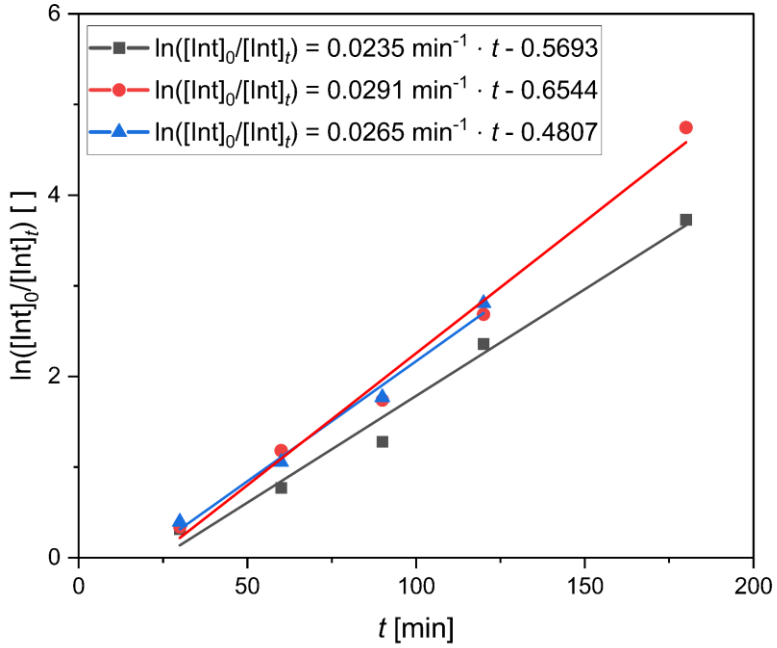

Fig. S68: Semilogarithmic plot of $\ln([Int]_0/[Int]_t)$ versus t for PLA methanolysis in THF with $[Fe(TMG_2e)Cl_2]$ (**C3**) at 60 °C (see Table S13 Entries 4–6).

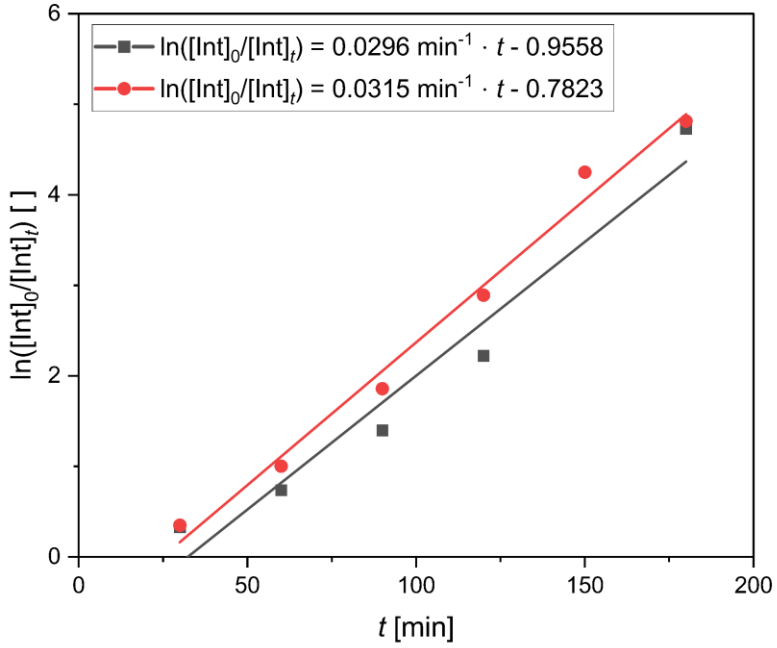

Fig. S69: Semilogarithmic plot of $\ln([Int]_0/[Int]_t)$ versus t for PLA methanolysis in THF with $[Fe(TMG_2p)Cl_2]$ (**C4**) at 60 °C (see Table S13 Entries 7 and 8).

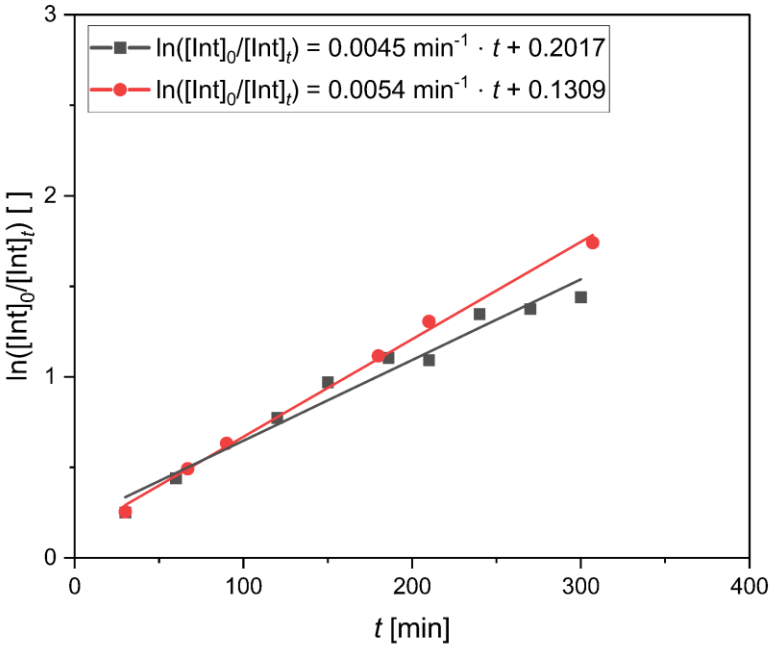

Fig. S70: Semilogarithmic plot of $\ln([Int]_0/[Int]_t)$ versus *t* for PLA methanolysis in THF with [Fe(TMG$_2$epy)Cl$_2$] (**C6)** at 60 °C (see Table S13 Entries 11 and 12).

8 DFT Calculations

8.1 Method

Density functional theory (DFT) calculations were performed with Gaussian 16, Revision B.01, using the default UltraFine grid (a 99,590 grid).[37] The TPSSh functional[38, 39] and the Ahlrichs type basis set def2-TZVP[40-42] were applied as implemented in Gaussian 16, Revision B.01[37]. As solvent model for MeCN, the polarizable continuum model (PCM) was used as implemented in Gaussian 16, Revision B.01. As empirical dispersion correction, the D3 version of Grimme's dispersion with Becke-Johnson damping (GD3BJ) was used as implemented in Gaussian 16, Revision B.01[43-45]. The structure optimizations were started from the molecular structures in the solid state. All subsequent calculations were performed based on the results of the optimization calculations. Frequency calculations did not show imaginary values. NBO calculations were performed using the program NBO 7.0 delivering the NBO charges and the charge-transfer energies by second order perturbation theory.[46-48] For the extraction of the calculated structural information, GaussView (Version 6.0.16) was used. The NBO results were extracted directly from the output files using notepad++ (Version 7.8.1).

The calculations were performed for the eight complexes of this work (**C1**–**C8**) and one complexes from a former publication of our group, namely [Fe(TMGqu)Cl_2] (**C9***)[49]. All calculations were carried out for the high-spin state (quintet) because the complexes exhibit typical bond lengths of iron(II) high-spin complexes. The results of the calculations are summarized in Table S14. For comparison, the experimental values determined by single-crystal X-ray diffraction are given in Table S15.

8.2 Results of DFT Calculations

Table S14: Results of DFT calculations of the herein presented iron(II) complexes **C1**–**C8** and the iron guanidine complex [Fe(TMGqu)Cl_2] (**C9***) from a previous work[49] (NBO 7.0, TPSSh/def2-TZVP, GD3BJ, PCM (MeCN)).

	C1	**C2**	**C3**	**C4**	**C5#**[a]	**C6**	**C7**	**C8**	**C9***
RMSD[b]	0.343	0.233	0.110	0.159	0.218	0.113	0.066	0.164	0.100
τ_4[c] / τ_5[d]	0.85	0.85	0.72	0.83	0.61	0.80	0.86	0.85	0.82
ρ[e]	0.98/ 0.98	0.99/ 0.98	0.96/ 0.96	0.97/ 0.97	0.97/ 0.97	0.97	0.98/ 0.98	0.98/ 0.99	0.99
NBO Charges [e units]									
Fe	1.25	1.24	1.24	1.28	1.30	1.27	1.24	1.23	1.26
$N_{gua,1}$	-0.69	-0.71	-0.69	-0.70	-0.68	-0.71	-0.71	-0.71	-0.69
$N_{gua,2}$	-0.69	-0.70	-0.69	-0.70	-0.68	–	-0.71	-0.71	–
$N_{py,1/qu,1}$	–	–	–	–	-0.52	-0.54	–	–	-0.51
$N_{py,2}$	–	–	–	–	-0.52	–	–	–	–
Cl_1	-0.74	-0.72	-0.75	-0.75	-0.72	-0.73	-0.74	-0.72	-0.73
Cl_2	-0.75	-0.75	-0.75	-0.76	–	-0.77	-0.74	-0.75	-0.74
Charge-transfer energies [kcal mol^{-1}]									
$N_{gua,1}$→Fe	42.0	47.1	49.1	43.3	47.7	52.3	38.8	44.8	41.2
$N_{gua,2}$→Fe	42.1	47.4	49.1	43.2	47.2	–	39.0	47.4	–
$N_{py/qu,1}$→Fe	–	–	–	–	40.0	41.4	–	–	42.7
$N_{py,2}$→Fe	–	–	–	–	39.9	–	–	–	–
Cl_1→Fe	93.3	100.2	84.8	83.3	95.4	95.4	90.3	97.5	96.7
Cl_2→Fe	85.5	83.8	84.8	80.4	–	76.0	90.3	86.8	88.5
Bond lengths [Å]									
Fe–$N_{gua,1}$	2.068	2.038	2.067	2.058	2.094	2.020	2.066	2.042	2.076
Fe–$N_{gua,2}$	2.068	2.045	2.067	2.058	2.092	–	2.066	2.035	–
Fe–$N_{py,2/qu,1}$	–	–	–	–	2.179	2.130	–	–	2.113
Fe–$N_{py,2}$	–	–	–	–	2.182	–	–	–	–
Fe–Cl_1	2.285	2.288	2.312	2.324	2.331	2.288	2.296	2.288	2.275
Fe–Cl_2	2.306	2.319	2.312	2.309	–	2.326	2.296	2.318	2.282

[a] Calculation was performed for the complex cation $[Fe(TMGpy)_2Cl]^+$ (**C5#**). [b] Root-mean-square deviation compared to the molecular structure experimentally determined by single-crystal X-ray diffraction. Calculated with the program Mercury.[50] [c] τ_4 = [360°−(α+β)]/141°; α and β are the largest angles in a complex with a fourfold coordinated metal center.[51] [d] τ_5= (β-α)/60°; α and β are the largest angles in a complex with a fivefold coordinated metal center with $\beta \geq \alpha$.[52] [e] Degree of delocalization within the guanidine moiety $\rho = 2a/(b+c)$ with $a = d(C{=}N_{gua})$ and $b,c = d(C{-}N_{amine})$.[34]

Table S15: Experimental bond lengths and structure parameters of complexes **C1**–**C8** and the iron guanidine complex [Fe(TMGqu)Cl_2] (**C9***) from a previous work[49].

	C1	**C2**	**C3**	**C4**	**C5**	**C6**	**C7**	**C8**	**C9*[a]**
					Structure Parameters				
τ_4[a] / τ_5[b]	0.89	0.90	0.73	0.81	0.68	0.85	0.88 / 0.88	0.84	0.83
ρ[c]	0.98/ 0.98	0.98/ 0.99	0.96/ 0.96	0.97/ 0.97	0.98/ 0.96	0.98	0.99/ 1.01 0.97/ 0.97	0.97/ 0.99	0.99
					Bond lengths [Å]				
Fe–$N_{gua,1}$	2.093(1)	2.051(2)	2.084(1)	2.055(2)	2.092(3)	2.021(3)	2.076(3)/ 2.073(3)	2.054(1)	2.069(2)
Fe–$N_{gua,2}$	2.068(1)	2.052(2)	2.084(1)	2.054(1)	2.072(2)	–	2.073(3)/ 2.073(3)	2.036(1)	–
Fe–$N_{py,2}$	–	–	–	–	2.218(3)	2.120(3)	–	–	2.086(2)
Fe–$N_{py,2}$	–	–	–	–	2.213(3)	–	–	–	–
Fe–Cl_1	2.269(1)	2.262(1)	2.286(1)	2.331(1)	2.327(1)	2.289(2)	2.261(2)/ 2.266(2)	2.264(1)	2.240(1)
Fe–Cl_2	2.278(1)	2.285(1)	2.286(1)	2.289(1)	–	2.253(2)	2.245(2)/ 2.266(2)	2.276(1)	2.252(1)

[a] τ_4 = [360°−(α+β)]/141°; α and β are the largest angles in a complex with a fourfold coordinated metal center.[51] [b] τ_5= (β-α)/60°; α and β are the largest angles in a complex with a fivefold coordinated metal center with $\beta \geq \alpha$.[52] [c] Degree of delocalization $\rho = 2a/(b+c)$ with $a = d$(C=N_{gua}) and $b,c = d$(C–N_{amine}).[34]

9 References

1. Mestrelab Research, *MestReNova* (12.0.1), Mestrelab Research, Santiago de Compostela, Spain, 2018.
2. H. E. Gottlieb, V. Kotlyar and A. Nudelman, *J. Org. Chem.*, 1997, **62**, 7512-7515.
3. STOE, *X-Area Pilatus3_SV* (1.31.131.0), STOE & Cie GmbH, Darmstadt, Germany, 2017.
4. STOE, *X-Area Pilatus3_SV* (1.31.170.0), STOE & Cie GmbH, Darmstadt, Germany, 2020.
5. STOE, *X-Area Integrate* (1.71.0.0), STOE & Cie GmbH, Darmstadt, Germany, 2016.
6. STOE, *X-Area Integrate* (1.78.3.0), STOE & Cie GmbH, Darmstadt, Germany, 2020.
7. STOE, *X-Area Recipe* (1.33.0.0), STOE & Cie GmbH, Darmstadt, Germany, 2015.
8. STOE, *X-Area Recipe* (1.36.0.0), STOE & Cie GmbH, Darmstadt, Germany, 2020.
9. STOE, *X-Area LANA* (1.71.4.0), STOE & Cie GmbH, Darmstadt, Germany, 2017.
10. STOE, *X-Area LANA* (1.83.8.0), STOE & Cie GmbH, Darmstadt, Germany, 2020.
11. Bruker, *XPREP* Bruker AXS Inc., Madison, WI, USA, 2007.
12. G. Sheldrick, *Acta Crystallogr., Sect. A*, 1990, **46**, 467-473.
13. G. Sheldrick, *Acta Crystallogr., Sect. A*, 2015, **71**, 3-8.
14. C. B. Hubschle, G. M. Sheldrick and B. Dittrich, *J. Appl. Crystallogr.*, 2011, **44**, 1281-1284.
15. G. Sheldrick, *Acta Crystallogr., Sect. C*, 2015, **71**, 3-8.
16. Shimadzu, *LabSolutions IR* (2.15), Shimadzu Corporation, Kyoto, Japan, 2016.
17. Y.-C. Huang, P. Tremouilhac, A. Nguyen, N. Jung and S. Bräse, *J. Cheminf.*, 2021, **13**, 8.
18. S. Hardy, I. M. de Wispelaere, W. Leitner and M. A. Liauw, *Analyst*, 2013, **138**, 819-824.
19. Kaiser Optical Systems, *iC Raman* (4.1.917 SP2), Kaiser Optical Systems Inc., Ann Arbor, MI, USA, 2009.
20. S-PACT, *PEAXACT* (5.7), S-PACT GmbH, Aachen, Germany, 2022.
21. NETZSCH, *NETZSCH Proteus -Thermal Analysis* (8.0.3), NETZSCH-Gerätebau GmbH, Selb, Germany, 2022.
22. Malvern, *OmniSEC* (5.12.467), Malvern Panalytical Ltd., Malvern, Worcestershire, UK, 2014.
23. A. Kowalski, A. Duda and S. Penczek, *Macromolecules*, 1998, **31**, 2114-2122.
24. M. Save, M. Schappacher and A. Soum, *Macromol. Chem. Phys.*, 2002, **203**, 889-899.
25. S. Herres-Pawlis, U. Flörke and G. Henkel, *Eur. J. Inorg. Chem.*, 2005, **2005**, 3815-3824.
26. H. Eilingsfeld, G. Neubauer, M. Seefelder and H. Weidincer, *Chem. Ber.*, 1964, **97**, 1232-1245.
27. M. Kawahata, K. Yamaguchi, T. Ito and T. Ishikawa, *Acta Crystallogr., Sect. E: Crystallogr. Commun.*, 2006, **62**, o3301-o3302.
28. V. Raab, J. Kipke, R. M. Gschwind and J. Sundermeyer, *Chem. Eur. J.*, 2002, **8**, 1682-1693.
29. H. Wittmann, A. Schorm and J. Sundermeyer, *Z. Anorg. Allg. Chem.*, 2000, **626**, 1583-1590.
30. S. Pohl, M. Harmjanz, J. Schneider, W. Saak and G. Henkel, *J. Chem. Soc., Dalton Trans.*, 2000, DOI: 10.1039/B002554M, 3473-3479.
31. A. Hoffmann, J. Börner, U. Flörke and S. Herres-Pawlis, *Inorg. Chim. Acta*, 2009, **362**, 1185-1193.

32. R. Wortmann, A. Hoffmann, R. Haase, U. Flörke and S. Herres-Pawlis, *Z. Anorg. Allg. Chem.*, 2009, **635**, 64-69.

33. M. Kawahata, K. Yamaguchi and T. Ishikawa, *Cryst. Growth Des.*, 2005, **5**, 373-377.

34. V. Raab, K. Harms, J. Sundermeyer, B. Kovačević and Z. B. Maksić, *J. Org. Chem.*, 2003, **68**, 8790-8797.

35. D. R. Witzke, PhD Thesis, Michigan State University, 1997.

36. P. McKeown, L. A. Román-Ramírez, S. Bates, J. Wood and M. D. Jones, *ChemSusChem*, 2019, **12**, 5233-5238.

37. M. J. Frisch, G. W. Trucks, H. B. Schlegel, G. E. Scuseria, M. A. Robb, J. R. Cheeseman, G. Scalmani, V. Barone, G. A. Petersson, H. Nakatsuji, M. C. X. Li, A. V. Marenich, B. G. J. J. Bloino, R. Gomperts, B. Mennucci, H. P. Hratchian, J. V. Ortiz, A. F. Izmaylov, J. L. Sonnenberg, D. Williams-Young, F. L. F. Ding, J. G. F. Egidi, A. P. B. Peng, T. Henderson, D. Ranasinghe, V. G. Zakrzewski, J. Gao, N. Rega, G. Zheng, W. Liang, M. Hada, M. Ehara, K. Toyota, R. Fukuda, J. Hasegawa, M. Ishida, T. Nakajima, Y. Honda, O. Kitao, H. Nakai, T. Vreven, K. Throssell, J. A. Montgomery, J. E. P. Jr., F. Ogliaro, M. J. Bearpark, J. J. Heyd, E. N. Brothers, K. N. Kudin, V. N. Staroverov, T. A. Keith, R. Kobayashi, J. Normand, K. Raghavachari, A. P. Rendell, J. C. Burant, S. S. Iyengar, J. Tomasi, M. Cossi, J. M. Millam, M. Klene, C. Adamo, R. Cammi, J. W. Ochterski, R. L. Martin, K. Morokuma, O. Farkas, J. B. Foresman and D. J. Fox, *Gaussian 16* (Revision B.01), Gaussian, Inc., Wallingford, CT, USA, 2016.

38. V. N. Staroverov, G. E. Scuseria, J. Tao and J. P. Perdew, *J. Chem. Phys.*, 2003, **119**, 12129-12137.

39. J. Tao, J. P. Perdew, V. N. Staroverov and G. E. Scuseria, *Phys. Rev. Lett.*, 2003, **91**, 146401.

40. K. Eichkorn, F. Weigend, O. Treutler and R. Ahlrichs, *Theor. Chem. Acc.*, 1997, **97**, 119-124.

41. F. Weigend and R. Ahlrichs, *Phys. Chem. Chem. Phys.*, 2005, **7**, 3297-3305.

42. A. Schäfer, C. Huber and R. Ahlrichs, *J. Chem. Phys.*, 1994, **100**, 5829-5835.

43. S. Grimme, S. Ehrlich and L. Goerigk, *J. Comput. Chem.*, 2011, **32**, 1456-1465.

44. L. Goerigk and S. Grimme, *Phys. Chem. Chem. Phys.*, 2011, **13**, 6670-6688.

45. A. Hoffmann, R. Grunzke and S. Herres-Pawlis, *J. Comput. Chem.*, 2014, **35**, 1943-1950.

46. F. Weinhold and C. R. Landis, *Valency and Bonding: A Natural Bond Orbital Donor-Acceptor Perspective*, Cambridge University Press, Cambridge, 2005.

47. E. D. Glendening, C. R. Landis and F. Weinhold, *J. Comput. Chem.*, 2019, **40**, 2234-2241.

48. E. D. Glendening, J. K. Badenhoop, A. E. Reed, J. E. Carpenter, J. A. Bohmann, C. M. Morales, P. Karafiloglou, C. R. Lan-dis and F. Weinhold, *NBO* (7.0), Theoretical Chemistry Institute, University of Wisconsin, Madison, WI, USA, 2018.

49. R. D. Rittinghaus, P. M. Schäfer, P. Albrecht, C. Conrads, A. Hoffmann, A. N. Ksiazkiewicz, O. Bienemann, A. Pich and S. Herres-Pawlis, *ChemSusChem*, 2019, **12**, 2161-2165.

50. CCDC, *Mercury* (2022.3.0), The Cambridge Crystallographic Data Centre, Cambridge, UK, 2022.

51. L. Yang, D. R. Powell and R. P. Houser, *Dalton Trans.*, 2007, DOI: 10.1039/B617136B, 955-964.

52. A. W. Addison, T. N. Rao, J. Reedijk, J. van Rijn and G. C. Verschoor, *J. Chem. Soc., Dalton Trans.*, 1984, DOI: 10.1039/DT9840001349, 1349-1356.